



# A variational approach to the fracture of brittle thin films subject to out-of-plane loading

A. Mesgarnejad<sup>a</sup>, B. Bourdin<sup>b</sup>, M.M. Khonsari<sup>a,\*</sup>

<sup>a</sup> Department of Mechanical Engineering, Louisiana State University, Baton Rouge, LA 70803, USA

<sup>b</sup> Department of Mathematics and Center for Computation & Technology, Louisiana State University, Baton Rouge, LA 70803, USA

## ARTICLE INFO

### Article history:

Received 16 December 2012

Received in revised form

29 April 2013

Accepted 11 May 2013

Available online 22 May 2013

### Keywords:

Variational approach to fracture

Brittle fracture

Thin films

Dimension reduction

## ABSTRACT

We address the problem of fracture in homogenous linear elastic thin films using a variational model. We restrict our attention to quasi-static problems assuming that kinetic effects are minimal. We focus on out-of-plane displacement of the film and investigate the effect of bending on fracture. Our analysis is based on a two-dimensional model where the thickness of the film does not need to be resolved. We derive this model through a formal asymptotic analysis. We present numerical simulations in a highly idealized setting for the purpose of verification, as well as more realistic micro-indentation experiments.

© 2013 Elsevier Ltd. All rights reserved.

## 1. Introduction

Thermal barrier coatings, thin-lubricant films, and electronic display devices are examples of applications in which the integrity of mechanical components depends largely on the integrity of a thin film of material applied on the surface of a substrate. The need to gain insight into the nature of thin films under various thermal and mechanical loadings has led to a large body of theoretical, experimental and numerical publications reviewed in detail in [Mishnaevsky and Gross \(2004\)](#) and [Lawn et al. \(2002\)](#). Classical fracture mechanics has been widely used in the past few decades, and the majority of published works deal with the determination of critical loading for a pre-existing crack, usually growing on a pre-defined path. Such an assumption may be too restrictive when dealing with real life applications in which the nucleation point may be unknown and multiple cracks may be interacting or growing along unknown paths. [Fig. 1](#), for instance, shows fracture patterns obtained during micro-indentation experiments and illustrates how qualitatively and quantitatively different crack patterns arise for different scales or material properties.

To treat the problem of pre-tensioned films subject to in-plane displacements, [Hutchinson and Suo \(1992\)](#) introduced a non-dimensional fracture driving force  $Z = G/E_e$ , where  $G$  is the elastic energy release rate and  $E_e$  is the stored elastic energy per unit volume of the material. Using this parameter, they were able to categorize different fracture patterns in thin films and, more specifically, showed cases where surface cracks occur or a network of channel fractures develops. More recently, in [Xia and Hutchinson \(2000\)](#) developed a two-dimensional membrane model and derived solutions for a single crack and a network of parallel cracks, as well as spiral cracks based on linear fracture mechanics. Some of these solutions were recovered through a variational approach in [Léon Baldelli et al. \(2013\)](#).

\* Corresponding author. Tel.: +1 2255789192; fax: +1 2255785924.

E-mail addresses: [amesga1@tigers.lsu.edu](mailto:amesga1@tigers.lsu.edu) (A. Mesgarnejad), [bourdin@lsu.edu](mailto:bourdin@lsu.edu) (B. Bourdin), [khonsari@me.lsu.edu](mailto:khonsari@me.lsu.edu) (M.M. Khonsari).

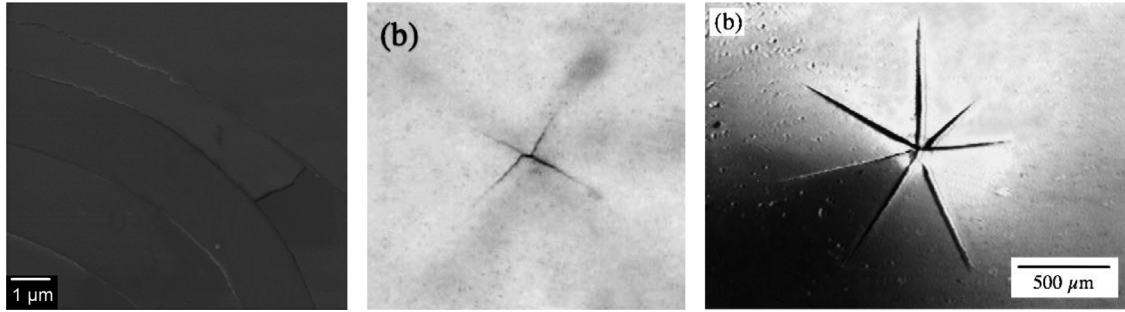


Fig. 1. Micro-indentation experiments reproduced from Sierras et al. (2011, Figure 3) (left) and Lawn et al. (2002, Figure 7–8) (center, right); reproduced with permission.

Our aim in this article is to examine the fracture of thin films with negligible thickness compared to the dimensions of the domain being analyzed, and in which transverse cracks span the entire cross-section of the film. We introduce a bulk energy consisting of two terms: the energy stored in the thin film and a Winkler foundation-type (Szilard, 2004) energy due to deformation in the bond between the thin film and the substrate. We justify these under specific scaling properties of the thickness and elastic properties of the film and bonding layers by an asymptotic analysis argument. This reduces the settings of our problem from three to two dimensions.

We propose to adopt the point of view of the variational approach to fracture mechanics (Francfort and Marigo, 1998; Bourdin and Chambolle, 2000; Bourdin, 2007; Bourdin et al., 2008), which we adapt to our specific situation, in order to eliminate the reliance on *a priori* knowledge of the crack path or morphology. We build upon the work of Léon Baldelli et al. (2013), but focus on the out-of-plane deformation of a film perfectly bonded to an elastic substrate. The postulated evolution law is based on sequences of *unilateral global minimization* of a total energy consisting of the sum of a bulk energy associated with the elastic deformation of the thin film away from cracks and the surface energy due to creation of transverse cracks. The assumption of cracks propagating in a quasi-static setting is consistent with our focus on the asymptotic limit of a film of vanishing thickness and on cracks that are long compared to the thickness of the film.

We propose a numerical approach based on a regularized energy similar to the one presented in Bourdin and Chambolle (2000). To verify our approach we focus on highly idealized situations, in particular in one-dimensional cases where exact solutions can be built. Using this relatively simple model, we are able to highlight several observed behaviors of cracks in thin films, including the nucleation of arrays of parallel cracks (see Sections 3 and 4.1), fracture branching, cell formation, and formation of networks of channel cracks (see Section 4.2).

The article is organized as follows. In Section 2.1, we give the elastic and fracture energies for a static problem, and derive a model for quasi-static evolutions in Section 2.2. In Section 2.3, we propose a non-dimensional formulation. In Section 2.4, we present our numerical approach. Section 3 is devoted to the verification of the numerical implementation in an idealized setting. In Section 4, we offer two more realistic numerical experiments highlighting the versatility of our formulation. Additionally, a numerical approach leading to an exact solution of the one dimensional problem is presented in Appendices A and B is devoted to the formal derivation of our reduced model.

## 2. Variational model for fracture of a thin film

### 2.1. Formulation of the problem

A host of problems arises in applications that are based on a reduced dimensional formulation. Plate and shell models, in theory of elasticity, are examples of such a dimension reduction. Here we are interested in one such problem with an elastic homogenous thin layer bonded to a substrate. For the engineering minded reader, this model is similar to a plate with an elastic foundation (Szilard, 2004).

We consider an elastic thin film bonded to the upper surface  $\Omega \subset \mathbb{R}^2$  of the substrate  $\mathcal{W} \subset \mathbb{R}^3$  by a Winkler type foundation. We denote the thin film's domain  $\Omega_f = \Omega \times (0, h) \subset \mathbb{R}^3$ . We focus on channel cracks  $\Gamma_f = \Gamma \times (0, h) \subset \mathbb{R}^2$  in the thin film. We consider loading through an imposed displacement at upper surface of the substrate namely  $w_t = w|_{\Omega \times \{0\}}$ . Intuitively, it is reasonable to assume that the thin film does not carry any vertical load and that its deformation is driven by the movement of substrate (Hutchinson and Suo, 1992). In all that follows, the displacement of the substrate–film interface is supposed to be known *a priori*.

To use the variational approach to fracture mechanics, the potential energy of the system must be calculated. Our model applies to situations where the dominant term in the elastic energy comes from bending effects. We account for a simplified configuration where the cohesive bond between the film and the substrate acts as an elastic highly anisotropic (essentially one-dimensional) medium (*i.e.*, a Winkler foundation). Rigorous validation of such a formulation requires examination of the three-dimensional elastic energies of the film and that of the cohesive bond when thicknesses of both layers approach zero. In fact, it is possible to rigorously derive the two-dimensional problem as a limit of a three-dimensional energy when

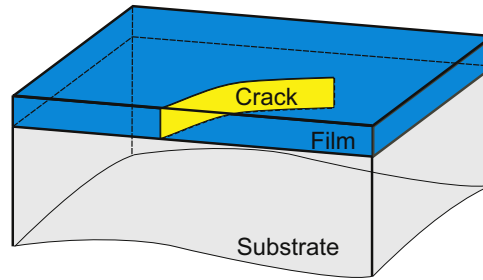


Fig. 2. Problem's schematics.

thickness of the film approaches zero ( $h \rightarrow 0$ ) using suitable scaling hypotheses. The derivation using asymptotic analysis can be found in [Appendix B](#) (Fig. 2).

**Remark 1.** The assumptions made while deriving the two-dimensional form of the energy translates to assumptions on the magnitude of the in and out-of-plane loadings. In terms of applications this implies:

- That thermal and residual stresses, as well as surface traction, are minimal. For cases like indentation of thin films this assumption seems valid since the in-plane normal stresses are largely due to the bending effects on the thin film.
- That the elastic modulus of the substrate in the vertical direction is small compared to its modulus in horizontal direction and also to that of the film. This applies to a film bonded on a compliant substrate such as the ones presented in [Sierros et al. \(2011\)](#) and [Rhee et al. \(2001\)](#).

Using [Appendix B](#), the expression for the bulk energy can be written as the sum of the bending energy of thin film plus that of the Winkler foundation. We can write the bulk energy of the film and cohesive bond for vertical displacement  $u \in H^2(\Omega \setminus \Gamma)$  of square integrable displacement fields with square integrable first and second derivatives as:

$$\begin{aligned} \mathcal{P}_t(u, \Gamma) &:= \int_{\Omega \setminus \Gamma} \mathcal{W}_b(u) dx + \int_{\Omega} \mathcal{W}_c(u, w_t) dx; \\ \mathcal{W}_b(u) &:= \frac{D}{2} W(D^2 u); \\ \mathcal{W}_c(u, w_t) &:= \frac{K}{2} (u - w_t)^2, \end{aligned} \quad (1)$$

where  $D^2$  represents the second derivative matrix defined as

$$D^2(v(x_1, x_2)) := \begin{bmatrix} v_{,11} & v_{,12} \\ v_{,12} & v_{,22} \end{bmatrix} \quad (2)$$

in two-dimensions, and where  $W$  is the elastic potential associated with any 2 by 2 matrix  $\Phi$  by

$$W(\Phi) := (\Phi_{11} + \Phi_{22})^2 - 2(1-\nu)(\Phi_{11}\Phi_{22} - \Phi_{12}^2), \quad (3)$$

and  $D$  and  $K$  are the flexural stiffness of the film and the modulus of the Winkler foundation is defined as

$$D := \frac{Eh^3}{12(1-\nu^2)} \quad (4)$$

where  $E, \nu$  are elastic modulus and Poisson's ratio for the thin film.

Following the variational approach to fracture mechanics, we model fracture as an energy-releasing mechanism, in which the energy released varies linearly with respect to the new surfaces formed. This is, in essence, the premise of Griffith's criterion. Since we use a reduced two-dimensional formulation, where we lump the changes in thickness, cracks are simply reduced to one-dimensional entities that go through the film thickness, *i.e.* form channel cracks. Hence, the energy release is assumed to be proportional to the crack surface area

$$S(\Gamma) := hG_c \mathcal{H}^1(\Gamma) \quad (5)$$

where  $\mathcal{H}^1$  is the one-dimensional Hausdorff measure (*i.e.*,  $\mathcal{H}^1(\Gamma_t)$  is the aggregate length of the cracks) and  $G_c$  is the critical elastic energy release rate associated with an infinitesimal increment of crack length.

Combining (1) with (5) yields the total potential energy

$$\mathcal{E}_t(u, \Gamma) := \mathcal{P}_t(u, \Gamma) + S(\Gamma) \quad (6)$$

### 2.2. Quasi-static evolution

Throughout this article, we focus on a quasi-static evolution. For a crack set  $\Gamma$ , the admissible displacement set consists of functions  $\mathcal{C}(\Gamma) := H^2(\Omega \setminus \Gamma)$ . The evolution of the displacement field and associated crack set for a given loading history  $w_t$  is given by the continuous evolution law (see Bourdin et al., 2008 for instance):

**Definition 1** (Quasi-static evolution). Given a loading sequence  $w_t$  for  $t \in [0, t_{max}]$ , a function  $t \rightarrow (u_t \in \mathcal{C}(\Gamma_t), \Gamma_t \subset \Omega)$  is the solution of quasi-static evolution if it satisfies

1. Irreversibility of the crack evolution:

$$\Gamma_t \supseteq \Gamma_s, \quad \forall 0 \leq s \leq t \tag{7}$$

2. Unilateral global stability. At any time  $t$ , the state  $(u_t \in \mathcal{C}(\Gamma_t), \Gamma_t)$  is the global minimizer of total energy among all admissible states:

$$\mathcal{E}_t(u_t, \Gamma_t) \leq \mathcal{E}_t(u, \Gamma), \quad \forall u \in \mathcal{C}_t(\Gamma_t), \quad \forall \Gamma \supseteq \Gamma_t \tag{8}$$

3. Energy balance. The function  $E(t) := \mathcal{E}_t(u_t, \Gamma_t)$  is absolutely continuous in  $t$  and satisfies the condition

$$E(t) - E(0) = - \int_0^t \int_{\Omega} \sigma_t \frac{\partial w_t}{\partial t} dx dt \tag{9}$$

where  $\sigma_t := K(u - w_t)$ .

Since the process is assumed to be rate-independent, evolution in time is only accounted through the irreversibility condition. Thus, it is easy to see that up to rescaling of time, any monotonically increasing load can be replaced with a linear scaling of a reference load

$$w_t = t w_0, \tag{10}$$

where the parameter  $t$  is merely a scaling factor; although this designation is admittedly imprecise, we occasionally refer to  $t$  as “time”.

### 2.3. Non-dimensionalization

We begin our analysis by providing a rescaled version of the total energy in Eq. (6). We consider the normalized space variable  $\tilde{x} := x/x_0$ , the normalized displacement  $\tilde{u} := u/u_0$ , and the normalized loading parameter  $\tilde{w}_t := w_t/u_0$ . In a similar fashion, we define  $\tilde{\Omega} = \Omega/x_0 := \{x/x_0; x \in \Omega\}$ , and  $\tilde{\Gamma} = \Gamma/x_0 := \{x/x_0; x \in \Gamma\}$ . Upon substituting the rescaled quantities in the expression of the total energy, we obtain

$$\frac{x_0^2}{u_0^2 D} \mathcal{E}_t(\tilde{u}, \tilde{\Gamma}) = \frac{1}{2} \int_{\tilde{\Omega} \setminus \tilde{\Gamma}} W(D^2 \tilde{u}) d\tilde{x} + \frac{1}{2} \frac{K x_0^4}{D} \int_{\tilde{\Omega}} (\tilde{u} - \tilde{w}_t)^2 d\tilde{x} + \frac{G_c h x_0^3}{u_0^2 D} \mathcal{H}^1(\tilde{\Gamma}) \tag{11}$$

In what follows, we set  $x_0 = u_0 = L$ , where  $L$  is some characteristic length of the domain  $\Omega$ . With this choice of parameters, we can rewrite (6) as

$$\tilde{\mathcal{E}}_t(\tilde{u}, \tilde{\Gamma}) := \frac{1}{2} \int_{\tilde{\Omega} \setminus \tilde{\Gamma}} W(D^2 \tilde{u}) d\tilde{x} + \frac{\tilde{K}}{2 \tilde{a}^4} \int_{\tilde{\Omega}} (\tilde{u} - \tilde{w})^2 d\tilde{x} + \frac{\tilde{G}}{\tilde{a}} \mathcal{H}^1(\tilde{\Gamma}) \tag{12}$$

where  $\tilde{K}$ , and  $\tilde{G}$ , and  $\tilde{a}$  are dimensionless parameters defined as

$$\begin{cases} \tilde{K} := \frac{12Kh(1-\nu^2)}{E}, \\ \tilde{G} := \frac{12G_c(1-\nu^2)}{Eh}, \\ \tilde{a} := \frac{h}{L}. \end{cases} \tag{13}$$

**Remark 2.** The actual choice of the normalization parameters  $x_0$  and  $u_0$  is arbitrary. Another possible choice, similar to the one adopted in Léon Baldelli et al. (2013), is  $x_0 = (D/K)^{1/4}$  and  $u_0 = \sqrt{G_c h x_0^3 / D}$  so that all coefficients in (11) become equal to 1. Our choice leads to the domain size and displacement magnitude of the order of 1 and is motivated by our focus on the numerical implementation, at the expense of slightly more complicated expressions.

For the sake of conciseness and in order to simplify the notation, from this point on we omit the tilde on all fields, *i.e.* we write  $u$  for  $\tilde{u}$  and so on.

#### 2.4. Numerical implementation

The variational approach to fracture frees itself from the need of an *a priori* knowledge of the crack path or specification of an additional *branching criterion*. Nevertheless, an implementation requires sophisticated numerical methods capable of dealing with free discontinuity problems. Specifically, the method requires performing the minimization of the total energy with respect to *any* kinematically admissible displacement field  $u$  and *any* cracks defined by a curve or set of curves  $\Gamma$ . The method is derived from the one presented in-depth in Bourdin et al. (2008) and references therein. In what follows, we give a brief overview of the method focusing on the necessary changes required to deal with the biharmonic problem and refer the interested reader to the aforementioned references for more details.

Following the approach pioneered in Ambrosio and Tortorelli (1990) for an image segmentation problem and studied in-depth in Braides (1998), we introduce a regularization parameter  $\eta > 0$  homogeneous to a length and a secondary variable  $\alpha$  taking its values in  $(0,1)$  to represent the presence of cracks (in a sense to be clarified further below). We define the regularized energy

$$\mathcal{E}_{t,\eta}(u, \alpha) := \mathcal{P}_t(u, \alpha) + \mathcal{S}_\eta(\alpha), \quad (14)$$

where

$$\mathcal{P}_t(u, \alpha) := \frac{1}{2} \int_{\Omega} (1-\alpha)^2 W(D^2 u) \, dx + \frac{K}{2a^4} \int_{\Omega} (u-w_t)^2 \, dx, \quad (15)$$

and

$$\mathcal{S}_\eta(\alpha) := \frac{3G}{8a} \int_{\Omega} \frac{\alpha}{\eta} + \eta |\nabla \alpha|^2 \, dx. \quad (16)$$

In the setting of the Mumford–Shah functional or of anti-plane shear, the behavior of the regularized problem can be rigorously established. More specifically, it can be shown that as  $\eta \rightarrow 0$ ,  $\mathcal{E}_{t,\eta}$  converges to  $\mathcal{E}_t$  in the sense of  $\Gamma$ -convergence. From there, it is easily seen that the global minimizer of  $\mathcal{E}_{t,\eta}$  converges to that of  $\mathcal{E}_t$  as  $\eta \rightarrow 0$ . Roughly speaking, as  $\eta \rightarrow 0$ , the displacement field minimizing (14) becomes arbitrarily close to that of minimizing (12), and that the  $\alpha$  field converges to 1 “near the jumps of  $u$ ” (*i.e.*, the cracks) and to 0 almost everywhere else. This  $\Gamma$ -convergence result can be extended further to encompass the entire discrete and then continuous time evolution (see Giacomini, 2005). These results are mathematically complex and we do not attempt to extend them to our setting. Instead, we assume that they hold in the case of a bi-harmonic bulk term and proceeded by induction. We believe that the numerical results presented further along in Sections 3 and 4 give credit to this assumption, even though, admittedly, they are no substitute for a formal proof.

The numerical implementation and, in particular, the minimization strategy of (14) is now regarded classical. Following Bourdin et al. (2008), by considering a discrete set of loading parameters  $t_i$  and for a given choice of the regularization parameter  $\eta$ , we seek sequences of minimizers of the regularized energy. At each time step, the crack growth condition (7) is accounted for through the addition of constraints on the field  $\alpha$ . Namely, for each  $t_i$ , we solve the following minimization problem:

$$(u_i, \alpha_i) = \arg \min_{\substack{u_i \in \mathcal{K}_A \\ \alpha_i \in \mathcal{A}_\epsilon(t_{i-1})}} \mathcal{E}_{t,\eta}(u, \alpha), \quad (17)$$

where  $\mathcal{K}_A(t_i)$  denotes the set of kinematically admissible displacements and  $\mathcal{A}$  is defined by

$$\mathcal{A}_\epsilon(\alpha) = \{x \in \Omega; \alpha(x) < 1-\epsilon\}, \quad (18)$$

and  $\epsilon$  is some arbitrarily small parameter.

The actual minimization of (14) is achieved using a combination of alternate minimizations and a backtracking algorithm. At each time step, we iterate minimization with respect to  $u$  and  $\alpha$  until the results converge. In this algorithm, the first step to obtain  $u$  is a simple convex problem which is implemented by solving the associated Euler–Lagrange equation (*i.e.*, the elasticity problem) using the method of finite differences. The second step to solve for  $\alpha$  is to apply a bounded Trust Region Newton minimization scheme for the discrete energy. Upon convergence of the alternate minimizations algorithm, we compare the results to all the previous loading steps in order to avoid settling on *some* local minimizers (see Bourdin, 2007 for more details on the backtracking idea). Of course, we cannot claim that this approach *always* leads to a global minimizer. In some situations, we were able to compute the actual global minimizer of the regularized energy using dynamic programming and compare the results with the outcome of our minimization strategy (see Section 3.2).

Our implementation relies on the distributed data structures and linear algebra provided by PETSc (Balay et al., 1997, 2010a,b), whereas the constrained optimization problems are solved using TAO (Munson et al., 2012).

The astute reader will also have noticed the similarity between the regularized functional (14) and non-local gradient damage (Pham et al., 2011) or phase field (Hakim and Karma, 2009; Henry and Levine, 2004; Karma and Lobkovsky, 2004) models. In these models, the regularization parameter is given a physical interpretation (*e.g.*, internal length, interaction distance). However, our approach is somewhat different. The parameter  $\eta$  is treated purely as a numerical artifact of the

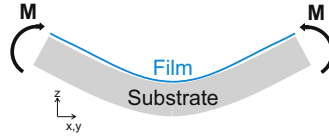


Fig. 3. Pure-bending problem schematic.

energy functional (14), which itself is treated as an intermediate expression in a two-step numerical method based on regularization followed by discretization. In short, our model is based on the minimization of a free discontinuity energy (12) and the specific form of its regularization (15) bears no special physical significance.

### 3. A one-dimensional verification problem

Under restrictive enough hypothesis on the loading, the geometry of the domain, and the structure of the solution, it is possible to build a closed-form (but non-trivial) solution of our model. This highly idealized situation provides valuable insight into the properties of the proposed model, and will allow us to provide some element of *verification* of our numerical implementation. We consider an elongated rectangular domain  $\Omega = \omega \times (-l_y/2, l_y/2)$  where  $\omega$  is some interval and  $l_y \ll 1$ , and assume that the loading function  $w_t$  depends only on  $x$  (Fig. 3).

In this situation, it is natural to consider only displacement fields that depend on  $x$  and transverse cracks in the form  $\Gamma = \gamma \times (-l_y/2, l_y/2)$  when  $\gamma$  consists of a discrete set of points in  $\omega$ . Introducing the function  $v_t := u - w_t$ , we define rescaled elastic, surface and total energies as

$$E_t(v_t, \gamma) := P_t(v_t, \gamma) + S(\gamma), \tag{19}$$

where one-dimensional bulk energy  $P_t$ , and one-dimensional surface energy  $S$  are defined as

$$P_t(v_t, \gamma) := \frac{1}{l_y} \mathcal{P}_t(u, \Gamma) = \frac{1}{2} \int_{\omega \setminus \gamma} (v_t'' + w_t'')^2 dx + \frac{K}{2a^4} \int_{\omega} v_t^2 dx, \tag{20}$$

$$S(\gamma) := \frac{1}{l_y} S(\Gamma) = \frac{G}{\alpha} \#(\gamma), \tag{21}$$

and  $\#(\gamma)$  denotes the counting measure of  $\gamma$  (i.e., the number of points in  $\gamma$ ).

In the 1-D case, we adopt a slightly different viewpoint by focusing on the film's fragments instead of its crack points. Given any interval  $\omega$ , we note that the choice of a countable family of  $n$  points  $\gamma = \{x_1, \dots, x_n\}$  is exactly equivalent to partitioning  $\omega$  into  $n+1$  disjoint open intervals  $\{\omega_0, \omega_1, \dots, \omega_n\}$  such that  $\omega_i \cap \omega_j = \emptyset$  if  $i \neq j$  and  $\bigcup_{0 \leq i \leq n} \overline{\omega_i} = \overline{\omega}$ . With a slight abuse of notation, for any such partition  $\mathcal{X} = \{\omega_0, \dots, \omega_n\}$  and any displacement field  $v_t$  twice differentiable in each  $\omega_i$  we define

$$E_t(v_t, \mathcal{X}) := P_t(v_t, \mathcal{X}) + S(\mathcal{X}), \tag{22}$$

where

$$P_t(v_t, \mathcal{X}) := \frac{1}{2} \sum_{i=0}^n \left[ \int_{\omega_i} (v_t'' + w_t'')^2 dx + \frac{K}{2a^4} \int_{\omega_i} v_t^2 dx \right] \tag{23}$$

$$S(\mathcal{X}) := \frac{G}{\alpha} [\#(\mathcal{X}) - 1]. \tag{24}$$

Hereafter, we focus on a specific choice of the loading function  $w_t(x) = -tx^2/2$  for which the elastic energy becomes

$$P_t(v_t, \mathcal{X}) = \frac{1}{2} \sum_{i=1}^{n+1} \left[ \int_{\omega_i} (v_t'' - t)^2 dx + \frac{K}{2a^4} \int_{\omega_i} v_t^2 dx \right]. \tag{25}$$

Despite its similarity with the problem of a homogeneous elastic membrane under constant in-plane strain studied in Xia and Hutchinson (2000) and Léon Baldelli et al. (2013), the minimization of  $E_t$  is much more challenging as we will see below.

#### 3.1. An explicit formula for the total energy of a film broken into $n+1$ fragments

We start our analysis by providing an explicit formula for the total energy of a film in elastic equilibrium. First, we write the elastic energy of a single fragment of length  $l$  free at both ends, noting that the modified elastic energy (25) is invariant by translation, so that the actual position of the fragment (i.e., choice of  $\mathcal{X}$ ) plays no role.

Consider an unfractured film occupying an interval  $\omega_k = (x_k, x_{k+1})$  of length  $l = x_{k+1} - x_k$ . Up to a translation, the modified displacement  $v_t$  is given by the minimizer of

$$P_t(v_t, \{(-l/2, l/2)\}) = \int_{-l/2}^{l/2} (v_t'' - t)^2 dx + \frac{K}{2a^4} \int_{-l/2}^{l/2} v_t^2 dx, \tag{26}$$

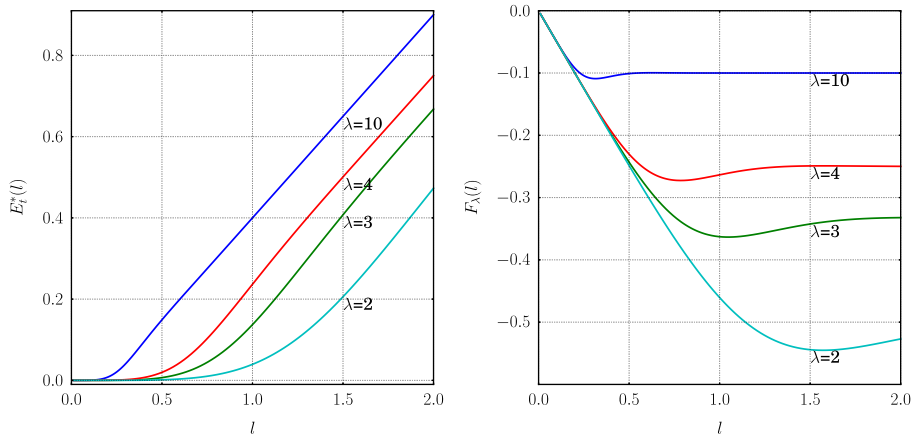


**Fig. 4.** Elastic energy (30) of fragment of length  $l$  with traction-free boundary conditions on both ends at unit load  $t=1$  (left) and scaling function  $F_\lambda(l)$  (31) (right) as a function of  $l$  for various values of  $\lambda$ .

leading to the Euler–Lagrange equations

$$v_t^{(4)} + \frac{K}{a^4} v_t = 0 \tag{27}$$

subject to the traction-free boundary conditions

$$v''_t(\pm l/2) = t, \quad v_t^{(3)}(\pm l/2) = 0. \tag{28}$$

After some tedious algebra, one obtains an explicit expression for the minimizing modified displacement

$$v_t^*(x) = \frac{2}{\lambda^2(\sin(\lambda l) + \sinh(\lambda l))} \left[ -\cos\left(\frac{\lambda l}{2}\right) \sinh\left(\frac{\lambda l}{2}\right) \sin(\lambda x) \sinh(\lambda x) + \sin\left(\frac{\lambda l}{2}\right) \cosh\left(\frac{\lambda l}{2}\right) \cos(\lambda x) \cosh(\lambda x) - \cos\left(\frac{\lambda l}{2}\right) \sinh\left(\frac{\lambda l}{2}\right) \cos(\lambda x) \cosh(\lambda x) - \sin\left(\frac{\lambda l}{2}\right) \cosh\left(\frac{\lambda l}{2}\right) \sin(\lambda x) \sinh(\lambda x) \right], \tag{29}$$

and for the associated elastic energy

$$E_t^*(l) := \frac{t^2}{2} (l + F_\lambda(l)), \tag{30}$$

where  $\lambda := K^{1/4}/a\sqrt{2}$  is an internal scaling factor that represents the ratio between cohesive energy and bending energy, and the function  $F_\lambda$  is defined by

$$F_\lambda(l) := \frac{2(\cos(\lambda l) - \cosh(\lambda l))}{\lambda(\sin(\lambda l) + \sinh(\lambda l))}. \tag{31}$$

Fig. 4 shows the elastic energy  $E_t^*(l)$  and function  $F_\lambda(l)$  as a function of the fragment length  $l$  for several values of the internal scaling factor  $\lambda$ . It is worth noting that the linear part of the energy is simply due to the work of imposed moments (i.e.,  $v''_t = t$ ) and the non-linear scaling function is due to the work of the modified displacement (i.e.,  $v_t^*$ ).

Using (30), it is easy to obtain a general formula for the total energy of a film broken into  $n+1$  fragments, summarized as follows.

**Proposition 1.** Consider a partition  $\mathcal{Y} = \{I_0, \dots, I_m\}$  of an interval  $I$ . Let  $v_t^*$  be the equilibrium modified displacement associated with the loading  $w_t(x) = -tx^2/2$ , i.e.,  $v_t^*|_{I_j} = \arg \min_v E_t(v, |I_j|)$ . Then, the total energy associated to  $\mathcal{Y}$  is

$$E_t^*(\mathcal{Y}) := E_t(v_t^*, \mathcal{Y}) = \frac{t^2}{2} \left( |I| + \sum_{j=0}^m F_\lambda(|I_j|) \right) + \frac{mG}{a}, \tag{32}$$

if  $m > 0$ , and

$$E_t^*(\mathcal{Y}) := E_t(v_t^*, I) = \frac{t^2}{2} (|I_0| + F_\lambda(|I_0|)) \tag{33}$$

otherwise.

In the case of the homogenous elastic membrane under constant in-plane strain in Léon Baldelli et al. (2013), a simple argument of convexity for the equivalent of  $F_\lambda$  leads to the conclusion that for a given value of  $n$ , the partition  $\mathcal{X}$  minimizing

$E_t^*(\mathcal{X})$  consists of  $n$  equal length fragments in  $\omega$ . Here,  $F_\lambda$  is non-convex and such a result does not hold true *a priori*, which renders obtaining a closed-form minimizer for  $E^*(t)$  much more challenging. Instead, we use a dynamic programming technique inspired by Chambolle (1995) to compute the true global minimizer of the total energy, and illustrate via examples that the optimal crack configuration may not result in fragments of equal length. In the next two sections, we use exact solutions obtained by a dynamic programming algorithm to verify the numerical implementation of the regularized functional (14). The details of this algorithm are presented in Appendix A.

### 3.2. Comparison with the elliptic regularization approach

A major hurdle is the stiffness of the elastic term in the regularized energy. Substituting  $\lambda$  in (15), it is clear that for small values of  $\lambda$ , the minimization of the total energy with respect to the displacement field becomes numerically ill-conditioned. Since realistic situations correspond to large values of the parameter  $\lambda$ , we chose to partially ignore this issue: we implemented a one dimensional version of the regularized energy by means of finite differences on a regular grid, which we used to replicate the experiments in Figs. A1 and A2. We then focused on the more realistic situations using two-dimensional finite differences.

In this section, we used the one-dimensional implementation of the regularized energy (14) for the problem in Fig. A1. Fig. 5 (left) compares each component of the fracture energy obtained with both methods, while the displacement  $v_t$  and fracture  $\alpha$  fields are plotted on the right, respectively, after the first and second crack nucleation ( $t=1, 2$ ). The space discretization consists of 800 grid points ( $\delta_x = 6.25 \times 10^{-4}$ ), while the loading interval  $0 \leq t \leq 3.0$  is discretized in 100 time steps and the regularization parameter is  $\eta = 10\delta_x$ . The backtracking algorithm from Bourdin (2007) was used in order to ensure energy balance at the crack nucleation loads. The agreement between both models, in terms of value of the energies, critical loads at nucleation and crack location is excellent.

In Fig. 6, the same process is repeated for the computation leading to an asymmetric crack pattern shown in Fig. A2. Here, the agreement is not as good. Whereas dynamic programming computations predict that single cracks should be nucleated respectively at  $x = -0.06, x = 0.22$ , and  $x = -0.28$  at  $t = 0.67, 0.73$ , and  $0.91$ , alternate minimizations of (14) lead to the nucleation of two symmetric cracks at  $x \approx \pm 0.09$  at  $t \approx 0.75$ , followed by the nucleation of two more cracks at  $x \approx \pm 0.24$  at  $t \approx 1.09$ . Fig. 6 (left) compares the total energy obtained with our dynamic programming algorithm (solid blue line) to that obtained through numerical minimization of (14), and highlights the difficulty of this problem. Note in particular how the solution with two symmetric cracks obtained with the alternate minimizations algorithm enhanced with the backtracking scheme is close to the global minimizer. Yet it appears to be a stable critical point of the regularized energy. Notice also how the optimal 3-crack configuration is not achievable from the two-crack configuration by virtue of irreversibility. This explains how the second bifurcation takes place at a higher loading value in the numerical simulation based on minimization of (14).

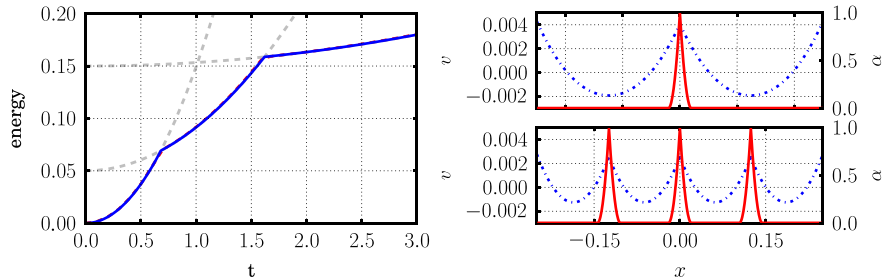


**Fig. 5.** Fracture of a one-dimensional sample uniformly loaded. Comparison between the dynamic programming solution from Fig. A1 and the minimization of the regularized energy (14) with  $\lambda = 10, l_0 = 0.5, G\alpha^{-1} = 0.05, \eta = 10\delta_x$ . Left: total energy as a function of the loading (blue solid line) compared to the dynamic programming solution (dashed lines). Right: displacement  $u$  (blue dotted line) and  $\alpha$  field (red solid line) at  $t=1.0$  (top) and  $t=2.0$  (bottom). (For interpretation of the references to color in this figure caption, the reader is referred to the online version of this article.)

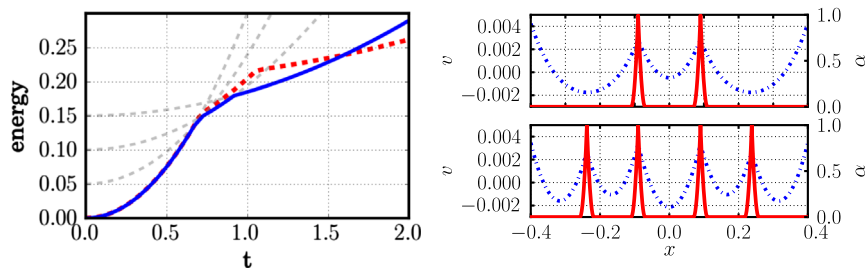


**Fig. 6.** Fracture of a one-dimensional sample uniformly loaded. Comparison between the dynamic programming solution from Fig. A2 and the minimization of the regularized energy (14) with  $\lambda = 10, l_0 = 0.8, G\alpha^{-1} = 0.05, \eta = 10\delta_x$ . Left: total energy as a function of the loading (blue solid line) compared to the dynamic programming solution (red dashed line). Right: displacement  $u$  (blue dotted line) and  $\alpha$  field (red solid line) at  $t=0.8$  (top) and  $t=1.5$  (bottom). (For interpretation of the references to color in this figure caption, the reader is referred to the online version of this article.)

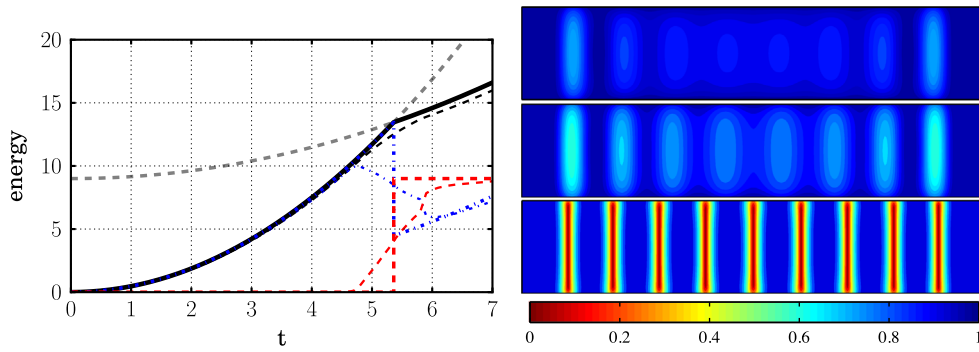


**Fig. 7.** Fracture of a two-dimensional sample under pure bending. Comparison between the dynamic programming solution from Fig. A4 and the minimization of the regularized energy (14) with  $\lambda = 31.6$ ,  $l_0 = 1$ ,  $Ga^{-1} = 1$ ,  $\eta = 5\delta x$ . Evolution of the energy (black: total, blue: surface energy) and comparison with the 1d global minimizer (thick lines) (top), fracture field  $\alpha$  at  $t = 5, 5.4, 5.8$  (from top to bottom). (For interpretation of the references to color in this figure caption, the reader is referred to the online version of this article.)

That the alternate minimizations algorithm fails to properly identify the proper solution is not a surprise, since it can only be shown to converge to a critical point of the energy. Thus, by virtue of its non-convexity, it may admit many local minimizers. In fact, whereas the variational approach to fracture postulates that crack nucleation is given by global minimizers of a non-convex energy, in the numerics what often triggers such events is the stability of the elastic solutions (see Pham et al., 2011). A continuation method, similar to the one implemented in Maurini et al. (2013) may be useful here, but was not tested, as we focused our attention towards more realistic situations.

We conclude this section by focusing on an example with more realistic parameters, which we can use for the verification of our two-dimensional finite difference implementation. We consider a two dimensional domain  $\Omega = (-0.5, 0.5) \times (-0.1, 0.1)$  discretized by a  $300 \times 60$  grid ( $\delta x = 3.3 \times 10^{-3}$ ). The internal scaling factor is  $\lambda = 31.6$ , and the regularization parameter is  $\eta = 5\delta x$ . Fig. 7 shows the comparison between the global minimizer of the energy  $\mathcal{E}_t$  obtained by dynamic programming and the energy of discrete regularized energy  $\mathcal{E}_{t,\eta}$ . The backtracking algorithm described in Bourdin et al. (2008) was used to avoid some classes of local minimizers and ensure energy balance.

As can be seen in Fig. 7, even with a relatively large regularization parameter  $\eta$ , the total energy of the numerical solution is very close to that of the global minimizer for the one-dimensional problem. Also note that the total energy obtained from two-dimensional numerical solution is smaller compared to that of the true one-dimensional global minimizer which can be attributed to the two-dimensional features near the boundary  $x_2 = \pm ly/2$  (see Fig. 7). Note also that while the surface and elastic energies of the numerical solutions are overall close to that of the global minimizer, one observes some discrepancy when the loading parameter  $t$  is such that  $4.5 \leq t \leq 6$ . This can be explained by two properties of our numerical solutions. Firstly, when  $4.5 \leq t \leq 6$ , our numerical solution is not the translation of a one-dimensional crack pattern (see in Fig. 7 how at the onset of nucleation, the cracks only span parts of the cross-section of our domain). Also, before crack nucleation, we observe that the  $\alpha$  field does not remain near 0. This leads to a softening effect similar to that of distributed damage. As the regularization parameter  $\eta$  becomes smaller, this effect should progressively vanish. For larger loads the fracture field  $\alpha$  remains overall near 0, with smooth but well-focused transitions to 1 at  $x = \pm 0.4, \pm 0.3, \pm 0.2, \pm 0.1, 0, 0$ , corresponding to the 9 cracks observed in the global minimizer (see Fig. A4).

#### 4. Numerical simulations

While the previous section is mostly concerned with verification of our implementation based on a highly idealized problems with little regard for the physical relevance of the rescaled material properties, we also focused on two more realistic problems. We first describe the fracture of a film coating on a cantilever beam then a spherical indentation of a film on compliant substrate.

##### 4.1. Coated cantilever beam

In order to simulate the transverse crack on a thin film coating a cantilever beam, we considered a rectangular domain  $\Omega = (0, l_x) \times (-ly/2, ly/2)$  subject to a substrate displacement  $w_t = tx^2(3l_x - x)$  corresponding to clamping the edge  $x=0$  and applying a point force of magnitude  $F = -t/6$  at  $x = l_x$  (Fig. 8). We chose for unit of length  $L = l_x$  in (12) so that our computational domain corresponds to a rectangle of unit length and height  $ly/l_x$ , which we discretized with a uniform grid of  $400 \times 40$  cells. We focused instead on the minimization of the regularized energy (14) over adapting the dynamic programming algorithm.

Fig. 9 shows snapshots of the fracture field a multiple increments of the loading parameter  $t$ . Again, we observe the progressive nucleation of an array of equidistant transverse cracks, growing from the clamped end towards the loaded end of the domain. The characteristic crack spacing appears to depend most strongly on the non-dimensional cohesive stiffness  $Ka^{-4}$ . Qualitatively, this behavior is similar to the one observed in Bourdin et al. (2008, Section 6) for the in-plane loading of

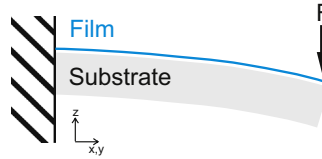


Fig. 8. Coated cantilever beam problem schematic.

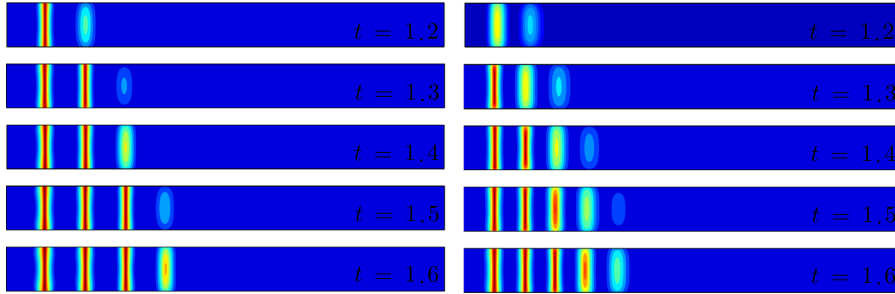


Fig. 9. Fracture of a two-dimensional coated cantilever beam with  $L=1.0$ ,  $Ga^{-1} = 1.$ ,  $\eta = 5\delta x$ : (left)  $Ka^{-4} = 6 \times 10^6$ , (right)  $Ka^{-4} = 1.2 \times 10^7$ .

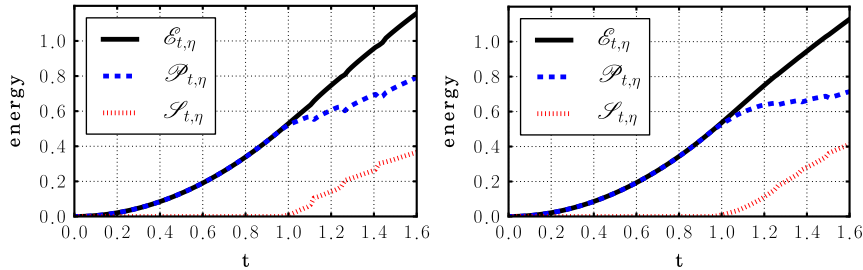


Fig. 10. Evolution of the elastic, surface and total energies for a two-dimensional coated cantilever beam with  $l_0=1.0$ ,  $Ga^{-1} = 1.$ ,  $\eta = 5\delta x$ : (left)  $Ka^{-4} = 6 \times 10^6$ , (right)  $Ka^{-4} = 1.2 \times 10^7$ .

a layered material. Fig. 10 shows the evolution of the elastic, surface and total energy for these two cases. Interestingly, it appears that after a loading phase during which the elastic energy grows as a quadratic function of the loading parameter, its growth become linear. This suggests that asymptotically, when the length of the domain becomes large compared to the crack spacing, the effective mechanical behavior associated with the growing network of parallel cracks is that of a damaged region growing from the left edge of the domain at the same rate.

#### 4.2. Indentation of thin films

We finally present numerical simulations indentation experiments of thin films, a truly two-dimensional problem of significant importance commonly used as testing methodology to measure different physical properties of thin films (Lawn, 1998; Mesarovic and Fleck, 1999; Morasch and Bahr, 2007). We considered a two-dimensional domain  $\Omega = (-0.5, 0.5)^2$  discretized by a structured mesh consisting of  $1500 \times 1500$  nodes ( $\delta x = 0.0025$ ) with regularization parameter  $\eta = 5\delta x = 0.005$ . We consider the action of a spherical indenter centered at  $(0, 0, R(1-t))$  from the film surface,  $t$  being as usual the loading parameter. Fig. 11 shows the settings of the problem. The displacement of the substrate is given by

$$W_t(x, y) = \begin{cases} 0 & \text{if } x^2 + y^2 \geq R^2 t(2-t), \\ R(1-t) + \sqrt{R^2 - x^2 - y^2} & \text{otherwise,} \end{cases}$$

*i.e.*, we neglect the deflection of the substrate unless it is in contact with the indenter. This is essentially similar to assuming a fully plastic substrate, and consistent with the experimental literature for very flexible substrate (Chai and Lawn, 2004; Sierros et al., 2011). Also since this loading is not monotonically increasing, we did not use the backtracking algorithm.

Fig. 12 shows snapshots of the evolution of the fracture field  $\alpha$  for increasing values of the loading parameter. The values for non-dimensional fracture toughness  $G = 5 \times 10^{-3}$  was calculated based on fracture toughness of Indium Tin Oxide (ITO) films as shown in Table 1 for a film of thickness  $h = 0.1 \mu\text{m}$ . The value of  $K$  was then calibrated based on the experimental observation. We did not attempt at performing a full quantitative comparison with experiments. However, features of our

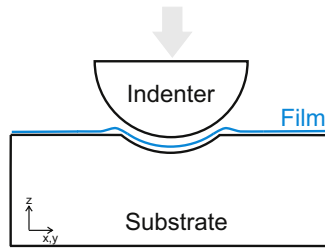


Fig. 11. Schematics of the micro-indentation problem.

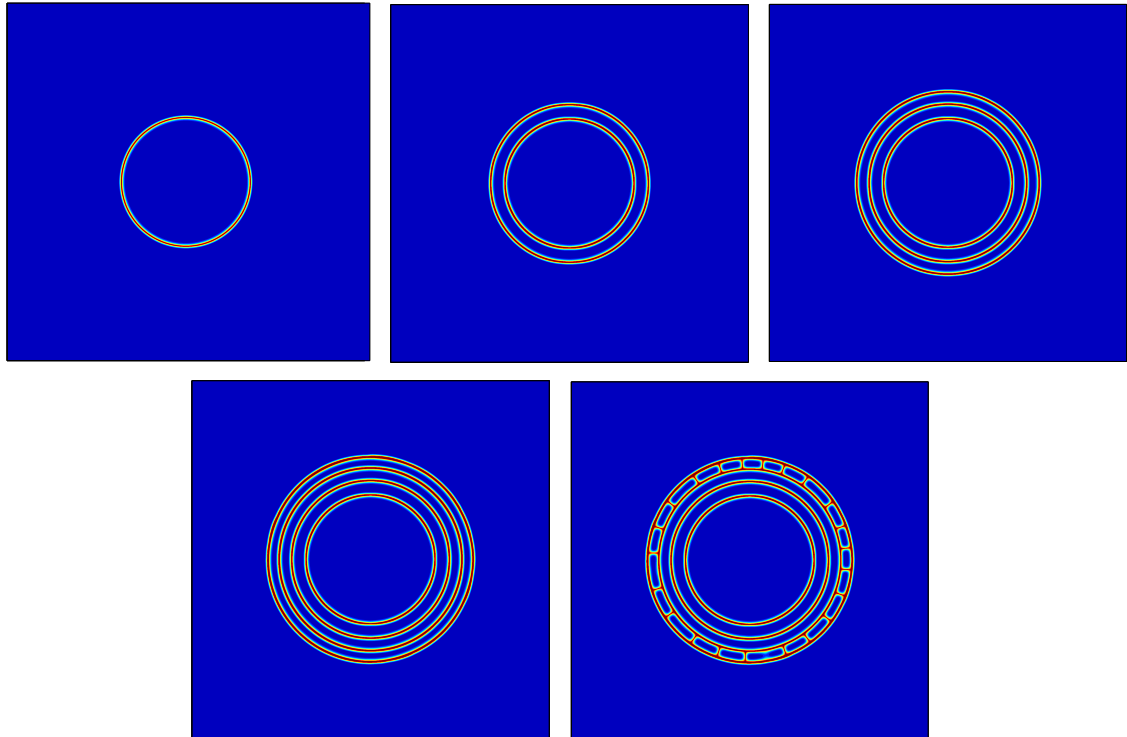


Fig. 12. Fracture of a two-dimensional thin-film with compliant substrate under spherical indenter of radius  $R=0.3$  with  $Ka^{-4} = 4 \times 10^6$ ,  $Ga^{-1} = 1$ , and  $\eta = 5\delta x$  at (from top left)  $t=0.3, 0.5, 0.7, 0.9, 1.0$ .

**Table 1**  
Physical properties of Indium Tin Oxide.

Young modulus (Zeng et al., 2003)	Critical stress intensity factor $K_{IC}$ (Chen, 2012)
$99.8 \pm 13.6$ GPa	$2.2 \pm 0.3$ MPa $\sqrt{m}$

numerical simulations compare favorably with experiments and common observations. In particular, the combination of circular cracks linked by smaller radial cracks was observed in Sierros et al. (2011, Fig. 3) reproduced here in Fig. 1.

Figs. 13 and 14 show sets of radial cracks obtained for two set of parameters corresponding to a thinner film or a larger indenter radius compared to that of the numerical experiments in Fig. 12. This cracks geometry is reminiscent of experiments presented in Lawn et al. (2002, Figs. 7 and 8), which were reproduced in Fig. 1. In an actual experiment, one observes that ring cracks evolve from the contact edge downward whereas radial cracks evolve from the interface upward. This behavior cannot be accounted for in our model as we assume that cracks always tunnel through the entire thickness of the film. Instead, we observe that cracks nucleate with a strictly positive length, which is consistent with the analysis of Chambolle et al. (2008). These cracks propagate with increasing load until the high values of  $t$  where ring cracks initiate at their outer radii. We can, however replicate some common observations of thin-film fracture; in particular, perpendicular crossing of fracture path in Fig. 13 and  $120^\circ$  branching of cracks in Fig. 14. Furthermore, in Fig. 14 one can see that as the non-dimensional fracture toughness of the film is reduced, there is transition from one branch (Fig. 14 (left)) to two very

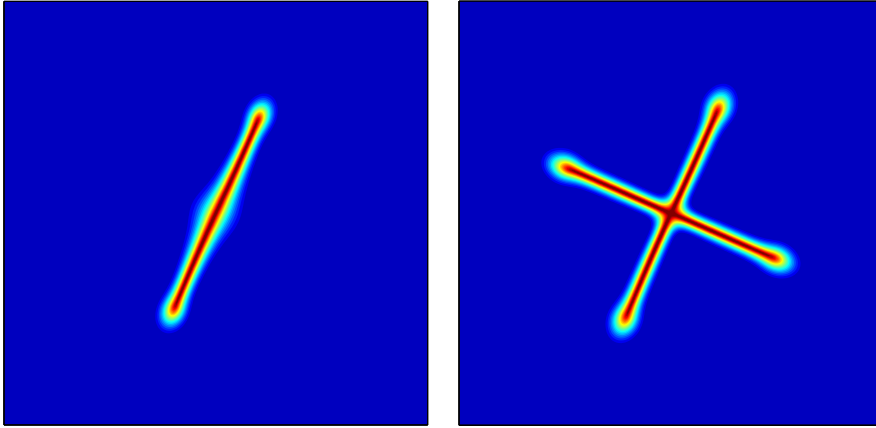


**Fig. 13.** Crossing of cracks in fracture of a two-dimensional thin-film with compliant substrate under spherical indenter of radius  $R=0.1$  zoomed to  $(-0.1, 0.1)^2$  with  $\eta = 5\delta x$  (from left)  $Ka^4 = 4 \times 10^6$ ,  $Ga^{-1} = 1$  at  $t=0.23$  (left),  $t=0.24$  (right).

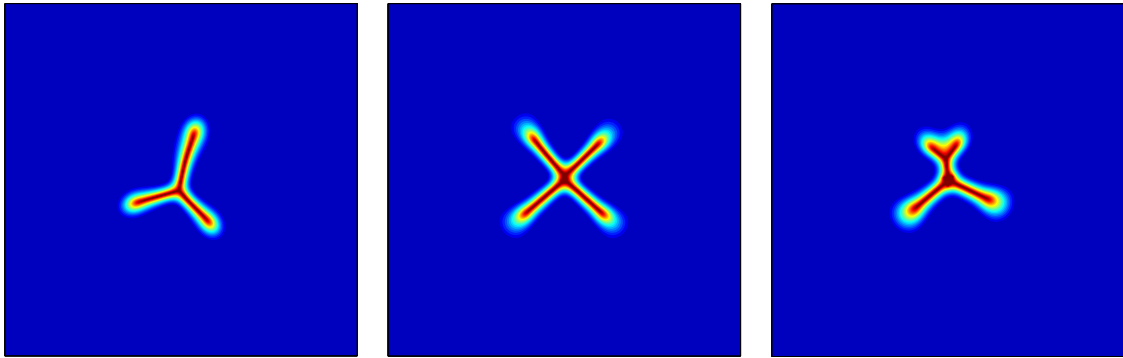


**Fig. 14.** Branching of cracks in fracture of a two-dimensional thin-film with compliant substrate under spherical indenter of radius  $R=0.1$  zoomed to  $(-0.1, 0.1)^2$  with  $\eta = 5\delta x$  (left)  $Ka^4 = 6.4 \times 10^7$ ,  $Ga^{-1} = 2.0$  at  $t=0.17$ , (center)  $Ka^4 = 6.4 \times 10^7$ ,  $Ga^{-1} = 1.5$  at  $t=0.1$  (right),  $Ka^4 = 6.4 \times 10^7$ ,  $Ga^{-1} = 0.7$  at  $t=0.075$ .

close branches (Fig. 14 (center)) and finally the distancing of the branching points (Fig. 14 (right)). This is similar to the observations made by Maurini et al. (2013) for drying driven fractures.

## 5. Conclusions

In this article, we extend the variational approach to fracture mechanics (Francfort and Marigo, 1998; Bourdin and Chambolle, 2000; Bourdin, 2007; Bourdin et al., 2008) to fracture of elastic thin films with elastic bonds to the substrate. The analysis is based on the bending effects in thin films in contrast to the available literature in this area where the focus is on in-plane effects (Xia and Hutchinson, 2000; Léon Baldelli et al., 2013).

The form of the total energy is obtained from three-dimensional linearized elasticity using asymptotic analysis under suitable assumptions in Appendix B. We also present an in-depth analysis of a highly idealized problem and verify our approach via numerical experiments. This is not easy since the analytical solution is only available in a few cases. In Section 3 we offer a case where it is possible to retrieve the *global minimizer* for quasi-static evolution. The results are compared to both one- and two-dimensional numerical experiments. Comparisons between the numerical results and predictions based on global minimality show that the regularization as offered in Section 2.4 converges to those predicted analytically.

We extend the numerical experiments in Section 4 to coated cantilever beams and spherical indentation of thin films to show different cases where the formulation can be applied. Two-dimensional loads, such as the ones offered here, lead to an intriguing array of phenomena (e.g. fracture networks, parallel fractures, spiral fracture patterns, fracture-made-cells, etc.). Specifically in Section 4.1 the numerical experiments offer an insight on existence of a second length scale (cracks spacing) different from the Griffith length scale that strongly depends on the non-dimensional cohesive stiffness  $Ka^4$ .

Although at this point we make no effort in quantitative validation of our model, in Section 4.2 we capture a wide range of observed phenomena in fracture of thin films on compliant substrates as well as thin-film fracture in general. These include transition of fracture patterns from circular to radial as well as branching and crossing of cracks.

The main objective of this work is to lay a solid background for the analysis of fracture in thin films. Variational approach to thin-film fracture mechanics shows its potential for prediction of crack nucleation and propagation path. Unlike other

methodologies in fracture mechanics by using variational approach to fracture mechanics, no *ad-hoc* treatment is necessary for crack nucleation or crack propagation and bifurcation. Instead, they are naturally predicted through minimization over all crack paths.

## Acknowledgments

A. Mesgarnejad and B. Bourdin wish to thank A.A. León Baldelli, J.-J. Marigo, and C. Maurini for their valuable help and support. B. Bourdin's work was supported in parts by the National Science Foundation under grant no. DMS-0909267. Some of the numerical experiments were performed using resources of the Extreme Science and Engineering Discovery Environment (XSEDE), which is supported by National Science Foundation grant no. OCI-1053575 under the Resource Allocation TG-DMS060014.

## Appendix A. A global minimization algorithm based on dynamic programming

Although the closed-form minimization of the total energy functional (32) is not feasible, it is possible to produce an algorithm that can be proven to converge to its *global* minimizer. This algorithm is derived from a dynamic programming approach devised in Chambolle (1995) for Mumford–Shah problem. It relies on the following key observation:

Consider a film occupying an interval  $\omega = (a, b)$  subject to a load of magnitude  $t$ , and let  $\mathcal{X}_\omega = \{\omega_0, \omega_1, \dots, \omega_m\}$  be the partition minimizing  $E_t^*(\bullet)$  amongst all partitions of  $\omega$ . Then  $\mathcal{X}^- := \{\omega_0, \omega_1, \dots, \omega_{m-1}\}$  minimizes  $E_t^*(\bullet)$  amongst all partitions  $\omega \setminus \omega_m$ , and

$$E_t^*(\mathcal{X}_\omega) = E_t^*(\mathcal{X}^-) + E_t^*((\omega_m)) + \frac{G}{a}. \quad (\text{A.1})$$

From there, it is easy to deduce that given any interval  $\omega = (a, b)$ ,

$$\min_{\mathcal{X} \text{ partition of } (a,b)} E_t^*(\mathcal{X}) = \min_{x_0 \in \omega} \left( \min_{\mathcal{X}^- \text{ partition of } (a,x_0)} E_t^*(\mathcal{X}^-) + E_t^*((x_0, b)) + \frac{G}{a} \right), \quad (\text{A.2})$$

and that the minimum on the right-hand-side of (A.2) is achieved by  $x_0$  and  $\mathcal{X}^-$ , then the minimum on the left hand side is achieved by  $\mathcal{X} := \mathcal{X}^- \cup (x_0, b)$ .

Noting finally that the energy is invariant by translation of the domain, *i.e.*, only the length of  $\omega$  matters, we arrive at the following algorithm:

**Algorithm 1.** Dynamic programming approach to the global minimization of (22) for a given loading parameter  $t$ .

- 1: assume  $\omega = (0, l)$  and let  $|\omega| = l$
- 2: for a given  $n_x$  define  $l_i = \frac{i}{n_x-1}l$
- 3: **for**  $i = n_x-1$  to 1 **do**
- 4:      $\mathcal{X}_{l_i}^1 \leftarrow \{(0, l-l_i)\}$
- 5:      $U_{l_i}^1 \leftarrow E_t^*(\mathcal{X}_{l_i}^1)$
- 6: **end for**
- 7:  $n_{\max} \leftarrow \frac{G E_t^*((0, l))}{t} + 1$
- 8: **for**  $n = 2$  to  $n_{\max}$  **do**
- 9:     **for**  $i = 1$  to  $n_x-1$  **do**
- 10:         Compute  $\mathcal{X}_i^n = \arg \min_{0 < j < i} (U_{l-l_j}^{n-1} + E_t^*(\mathcal{X}_i^1))$
- 11:          $U_i^n \leftarrow E_t^*(\mathcal{X}_i^n)$
- 12:     **end for**
- 13: **end for**
- 14: Compute  $\mathcal{X}^* := \arg \min_{1 \leq n \leq n_{\max}} U_l^n$
- 15:  $U^* \leftarrow E_t^*(\mathcal{X}^*)$

Considering quasi-static loading, and for a loading discretization  $\{t_i\}$ ,  $0 \leq i \leq N$ ,  $t_0 = 0$ ,  $t_N = T$ , if we assume  $\mathcal{X}^{(i)} := \{\omega_0^{(i)}, \dots, \omega_{m_i}^{(i)}\}$  is the optimal partition for film  $\omega = (a, b)$  at loading  $t_i$  then admissible partition at loading  $t_{i+1}$  consists of the union of optimal partitions of each  $\omega_j^{(i)}$ ,  $0 \leq j \leq m_i$ . This, in turn, enforces the irreversibility condition (IR) for each loading step.

Using the above observation we adapt this algorithm to account for the quasi-static evolution and the irreversibility constraint. Algorithm 2 finds the global minimizer partition  $\mathcal{X}_{(t_i)}^*$  of Eq. (22) for a monotonically increasing load at each step:

**Algorithm 2.** Dynamic programming approach to the global minimization of (22) under monotonically increasing load

- 1: Initiate  $\mathcal{X}_{(t_1)}^* = \{(0, l)\}$
- 2: Define  $\mathcal{P}(\omega) :=$  set of all partitions of  $\omega$
- 3: **for**  $i = 1$  to  $N$  **do**

```

4:   assume  $\mathcal{X}_{(i-1)}^* = \{\omega_1^{(i-1)}, \dots, \omega_n^{(i-1)}\}$  and let  $n \leftarrow \#(\mathcal{X}^{(i-1)})$ 
5:   for  $j=1$  to  $n$  do
6:      $\mathcal{Y}_j = \arg \min_{\mathcal{Y}_j \in \mathcal{P}(\omega_j^{(i-1)})} E_t^*(\mathcal{Y}_j)$  (using Algorithm 1)
7:   end for
8:    $\mathcal{X}_{(i)}^* \leftarrow \bigcup \{(\omega \in \mathcal{Y}_j; 1 \leq j \leq n)\}$ 
9:    $U_{(i)}^* \leftarrow E_t^*(\mathcal{X}_{(i)}^*)$ 
10:  end for

```

A.1. Numerical results using dynamic programming

Here we present two sets of results obtained using the dynamic programming Algorithm 2. The first set of results are from a set of parameters where the global minimizer of (22) similar to that of Léon Baldelli et al. (2013) is attained by fracture by bisection. The second set of results on the other hand highlights the effect of non-convexity of (22) resulting in an asymmetrical fracture pattern.

Fig. A1 shows the evolution of the total energy  $E_t^*$  (left) and a schematic representation of the cracks' locations (right) for the 1-D problem as a function of the loading parameter  $t$  for a domain of length  $l_0 = 0.5$  with  $\lambda = 10$ , and  $Ga^{-1} = 0.05$ .

At  $t=0.68$ , the configuration corresponding to a single crack at the center of the domain ( $x=0$ ) becomes energetically favored over the uncracked one. This is illustrated by the crossing of the energy curves corresponding, respectively, to the un-cracked configuration and the one with a single centered crack in Fig. A1 (left). A similar process takes place at  $t=1.62$  when the configuration associated with 3 equi-distributed cracks ( $x = -0.25, 0, 0.25$ ) becomes energetically less costly than the one with a single centered crack. This evolution by successive bisections is similar to the one observed in Léon Baldelli et al. (2013) in the case of constant in-plane strain.

On a longer domain, the non-convexity of the function  $F$  leads to a loss of symmetry. Fig. A2 represents the outcome of a numerical simulation similar to that of Fig. A1 with  $l_0 = 0.8$ . In this situation, the first crack nucleation at  $t=0.67$  is off-center at  $x = -0.06$ . Successive crack nucleations take place at the center of each ligament, but are staggered in time at  $t=0.73$ ,  $x=0.22$  and  $t=0.91$ ,  $x=-0.28$ . Note that Fig. A2 depicts one of the two solutions of this problem, the other being obtained by symmetry with respect to the domain center.

The link between non-convexity of the elastic energy functional and loss of symmetry can be easily seen from the graph of  $F_\lambda$  (31). From (32), it is easy to see that finding the optimal configuration consisting of a single crack is equivalent to solving the one-dimensional minimization problem

$$\min_{0 \leq l \leq l_0} F_\lambda(l) + F_\lambda(l_0 - l).$$

From the shape of the graph of  $F$  in Fig. 4, one would indeed expect that for small values of  $l_0$ ,  $F_\lambda(l) + F_\lambda(l_0 - l)$  admits a unique global minimizer at  $l_0/2$  whereas when  $l_0$  becomes larger, it becomes a “two-well” function and admits two global minimizers. This is illustrated in Fig. A3 where  $F_\lambda(l) + F_\lambda(l_0 - l)$  is plotted for  $\lambda = 10$  and  $l_0 = 0.5, 0.8$ . The non-convexity for  $l_0 = 0.8$  is made more obvious in the rightmost graph by zooming in around the origin.

In practical applications, the parameter  $\lambda$  is expected to be very large. Fig. A4 represents a summary of the crack evolution for a more realistic set of parameters:  $l_0 = 1$ ,  $\lambda = 31.62$ , and  $Ga^{-1} = 1$ . We chose the scaling factor so that upon a critical load, 9 equi-distributed cracks nucleate together  $\gamma = \{\pm 0.4, \pm 0.3, \pm 0.2, \pm 0.1, 0\}$ . Again, the qualitative difference between this evolution and the recursive subdivision observed in Léon Baldelli et al. (2013) comes from the non-convexity of the elastic energy with respect to the fragment length.

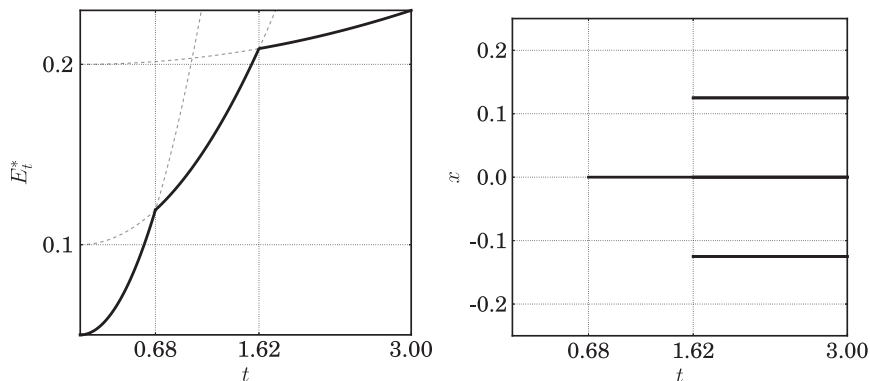


Fig. A1. Optimal energy (left) and crack location (right) of a sample of length  $l_0 = 0.5$  under pure bending obtained using dynamic programming algorithm with  $Ga^{-1} = 0.05$ ,  $\lambda = 10$ .

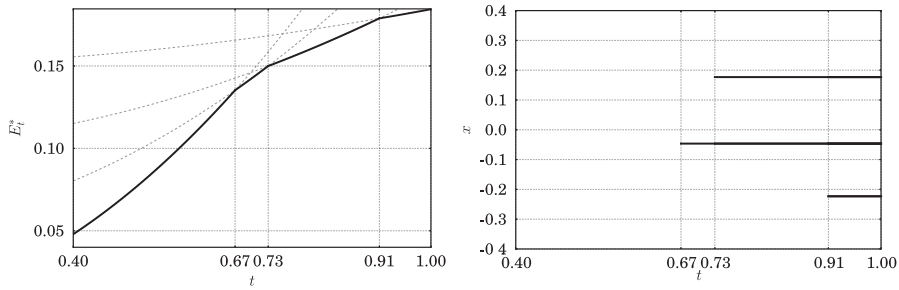


Fig. A2. Optimal energy (left) and crack location (right) of a sample of length  $l_0=0.8$  under pure bending obtained using dynamic programming algorithm with  $Ga^{-1} = 0.05, \lambda = 10$ .

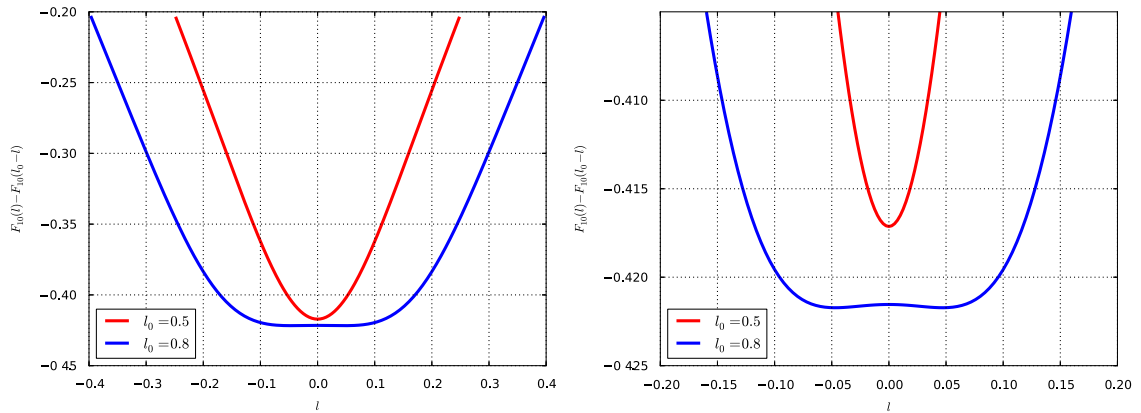


Fig. A3. Elastic energy of a configuration with a single crack as a position of its location, for a domain length  $l_0 = 0.5$  and  $l_0 = 0.8$ . In order to make comparisons easier, the graphs are shifted towards the left by  $l_0/2$ .

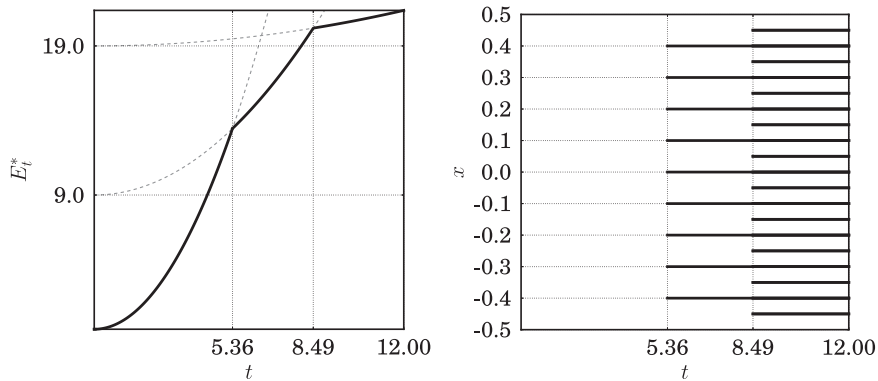


Fig. A4. Optimal energy (left) and crack location (right) of a sample of length  $l_0 = 1$  under pure bending obtained using dynamic programming algorithm with  $Ga^{-1} = 1, \lambda = 31.62$ .

**Appendix B. Derivation of the lower dimensional model**

We show how the reduced-dimension expression of the elastic energy can be formally derived from the full three dimensional model using a proper rescaling of the layers' thicknesses and elastic properties. We focus on the case of non-homogenous boundary condition i.e.,  $u^\epsilon = (0, 0, \bar{g}^\epsilon(x_1^\epsilon, x_2^\epsilon))$  at lower boundary of cohesive bond layer. We use the convention that greek letter subscripts stand for indices 1, 2 and latin letters for 1, 2, 3.

We consider a film of thickness  $\epsilon$  occupying a region  $\Omega_\epsilon := \omega \times (0, \epsilon)$  where  $\omega \subset \mathbb{R}^2$  and a transversely anisotropic bonding layer occupying  $\Omega'_\epsilon := \omega \times (-\epsilon, 0]$ .

The Hooke's law of the film and the bonding layers are given respectively for any kinematically admissible displacement field  $u^\epsilon$  by

$$\sigma_{ij}^\epsilon(u^\epsilon) := \lambda_\epsilon e_{kk}^\epsilon(u^\epsilon) \delta_{ij} + 2\mu e_{ij}^\epsilon(u^\epsilon), \tag{B.1}$$

and

$$\begin{cases} \sigma_{\alpha\beta}^\epsilon(u^\epsilon) := [\lambda'_\epsilon e_{\alpha\alpha}^\epsilon(u^\epsilon) + \lambda''_\epsilon e_{33}^\epsilon(u^\epsilon)] \delta_{\alpha\beta} + 2\mu'_\epsilon e_{\alpha\beta}^\epsilon(u^\epsilon) \\ \sigma_{\alpha 3}^\epsilon(u^\epsilon) := 2\mu''_\epsilon e_{\alpha\beta}^\epsilon(u^\epsilon) \\ \sigma_{33}^\epsilon(u^\epsilon) := \lambda''_\epsilon e_{kk}^\epsilon(u^\epsilon) + 2\mu'' e_{33}^\epsilon(u^\epsilon). \end{cases} \tag{B.2}$$

The total energy associated with  $u^\epsilon(x^\epsilon)$  in the film and bonding layer is then given by

$$E_\epsilon(u_\epsilon) = \frac{1}{2} \int_{\Omega_\epsilon \cup \Omega'_\epsilon} \sigma_\epsilon(u^\epsilon) : e_\epsilon(u^\epsilon) dx^\epsilon \tag{B.3}$$

Using a change of variables  $v^\epsilon = u^\epsilon - (0, 0, \bar{g}^\epsilon)$  where

$$g^\epsilon(x_1^\epsilon, x_2^\epsilon, x_3^\epsilon) = \begin{cases} 0 & \text{if } x^\epsilon \in \Omega_\epsilon \\ -x_3^\epsilon \bar{g}^\epsilon(x_1^\epsilon, x_2^\epsilon) & \text{if } x^\epsilon \in \Omega'_\epsilon \end{cases} \tag{B.4}$$

is the extension of  $\bar{g}^\epsilon$  to  $\Omega_\epsilon \cup \Omega'_\epsilon$ , we can write (B.3) as

$$E_\epsilon(v^\epsilon) = \frac{1}{2} \int_{\Omega_\epsilon \cup \Omega'_\epsilon} \sigma_\epsilon(v^\epsilon + g^\epsilon) : e_\epsilon(v^\epsilon + g^\epsilon) dx^\epsilon := J_\epsilon(v^\epsilon) + J'_\epsilon(v^\epsilon, \bar{g}^\epsilon), \tag{B.5}$$

Using the expression of the Hooke's laws, (B.5) can be rewritten as

$$\begin{aligned} J_\epsilon(v^\epsilon) := & \frac{1}{2} \int_{\Omega_\epsilon} \lambda e_{\alpha\alpha}^\epsilon(v^\epsilon) e_{\beta\beta}^\epsilon(v^\epsilon) + 2\mu e_{\alpha\beta}^\epsilon(v^\epsilon) e_{\alpha\beta}^\epsilon(v^\epsilon) dx^\epsilon + \frac{1}{2} \int_{\Omega_\epsilon} \lambda e_{\alpha\alpha}^\epsilon(v^\epsilon) e_{33}^\epsilon(v^\epsilon) + 4\mu e_{\alpha 3}^\epsilon(v^\epsilon) e_{\alpha 3}^\epsilon(v^\epsilon) dx^\epsilon \\ & + \frac{1}{2} \int_{\Omega'_\epsilon} (\lambda + 2\mu) e_{33}^\epsilon(v^\epsilon) e_{33}^\epsilon(v^\epsilon) dx^\epsilon, \end{aligned} \tag{B.6}$$

and

$$\begin{aligned} J'_\epsilon(v^\epsilon, \bar{g}^\epsilon) := & \frac{1}{2} \int_{\Omega'_\epsilon} \lambda' e_{\alpha\alpha}^\epsilon(v^\epsilon) e_{\beta\beta}^\epsilon(v^\epsilon) + 2\mu' e_{\alpha\beta}^\epsilon(v^\epsilon) e_{\alpha\beta}^\epsilon(v^\epsilon) dx^\epsilon + \frac{1}{2} \int_{\Omega'_\epsilon} \lambda'' e_{\alpha\alpha}^\epsilon(v^\epsilon) (e_{33}^\epsilon(v^\epsilon) - \bar{g}^\epsilon) dx^\epsilon \\ & + \frac{1}{2} \int_{\Omega'_\epsilon} 4\mu'' \left( e_{\alpha 3}^\epsilon(v^\epsilon) - \frac{x_3^\epsilon}{2} \bar{g}^\epsilon \right) \left( e_{\alpha 3}^\epsilon(v^\epsilon) - \frac{x_3^\epsilon}{2} \bar{g}^\epsilon \right) dx^\epsilon \\ & + \frac{1}{2} \int_{\Omega'_\epsilon} (\lambda'' + 2\mu'') (e_{33}^\epsilon(v^\epsilon) - \bar{g}^\epsilon) (e_{33}^\epsilon(v^\epsilon) - \bar{g}^\epsilon) dx^\epsilon. \end{aligned} \tag{B.7}$$

We then introduce the classical (see Ciarlet, 1997 for instance) scaling of the coordinate system and deformations

$$(x_\alpha, x_3) := (x'_\alpha, \frac{1}{\epsilon} x'_3), \quad (v_\alpha, v_3) := (v'_\alpha, \epsilon v'_3) \tag{B.8}$$

leading to the classical transformation of strains

$$\begin{cases} e_{\alpha\beta}(v) := e_{\alpha\beta}^\epsilon(v^\epsilon) \\ e_{\alpha 3}(v) := \epsilon e_{\alpha 3}^\epsilon(v^\epsilon) \\ e_{33}(v) := \epsilon^2 e_{33}^\epsilon(v^\epsilon). \end{cases} \tag{B.9}$$

Also to satisfy consistency of the order of magnitudes of  $\epsilon$  for displacement field components, we suppose that  $\bar{g} = \epsilon^2 \bar{g}^\epsilon$ .

The specific form of the linear elastic energy considered in this article can be derived under the assumption that the in-plane elastic moduli of the bonding layer are small compared to that of the film, and that the out of plane moduli are small compared to the in plane ones. Namely, we assume that

$$\begin{aligned} (\lambda_\epsilon, \mu_\epsilon) &:= (\lambda, \mu) \\ (\lambda'_\epsilon, \mu'_\epsilon) &:= \epsilon^2 (\lambda', \mu') \\ (\lambda''_\epsilon, \mu''_\epsilon) &:= \epsilon^4 (\lambda'', \mu''). \end{aligned} \tag{B.10}$$

Furthermore, we assume that the loading is such that  $\bar{g} = \epsilon^2 \bar{g}^\epsilon$  so that the total energy is of order  $\epsilon$ , and define

$$F_\epsilon(v) := \frac{E_\epsilon(v)}{\epsilon} = G_\epsilon(v) + G'_\epsilon(v, \bar{g}), \tag{B.11}$$

with

$$G_\epsilon(v) := \frac{1}{2} \int_{\Omega_1} \lambda e_{\alpha\alpha}(v) e_{\beta\beta}(v) + 2\mu e_{\alpha\beta}(v) e_{\alpha\beta}(v) dx$$

$$+ \frac{1}{2\epsilon^2} \int_{\Omega_1} 2\lambda e_{\alpha\alpha}(v) e_{33}(v) + 4\mu e_{\alpha 3}(v) e_{\alpha 3}(v) dx + \frac{1}{2\epsilon^4} \int_{\Omega_1} (\lambda + 2\mu) e_{33}(v) e_{33}(v) dx, \quad (\text{B.12})$$

and

$$\begin{aligned} G_\epsilon'(v, \bar{g}) := & \frac{\epsilon^2}{2} \int_{\Omega_1} \lambda' e_{\alpha\alpha}(v) e_{\beta\beta}(v) + 2\mu' e_{\alpha\beta}(v) e_{\alpha\beta}(v) dx \\ & + \frac{\epsilon^2}{2} \int_{\Omega_1} 2\lambda' e_{\alpha\alpha}(v) (e_{33}(v) - \bar{g}) dx + \frac{\epsilon^2}{2} \int_{\Omega_1} 4\mu' \left( e_{\alpha 3}(v) - \frac{x_3}{2} \bar{g}_{,\alpha} \right) \left( e_{\alpha 3}(v) - \frac{x_3}{2} \bar{g}_{,\alpha} \right) dx \\ & + \frac{1}{2} \int_{\Omega_1} (\lambda' + 2\mu') (e_{33}(v) - \bar{g}) (e_{33}(v) - \bar{g}) dx, \end{aligned} \quad (\text{B.13})$$

where, for the sake of conciseness, for  $\epsilon = 1$  we write  $\Omega_1 = \Omega_{\epsilon=1}$ ,  $\Omega'_1 = \Omega'_{\epsilon=1}$  are the rescaled domains.

Consider now a minimizer  $v$  of  $F_\epsilon$ , and the set  $\mathbb{V}$  of admissible test functions  $\mathbb{V} := \{\phi \in H^1(\Omega_1 \cup \Omega'_1); \phi(x_\alpha, -1) = 0\}$ . The first order optimality conditions for  $F_\epsilon$  become

$$A_\epsilon(v, \phi; \epsilon) + A'_\epsilon(v, \phi; \epsilon) = 0 \quad \forall \phi \in \mathbb{V} \quad (\text{B.14})$$

with

$$\begin{aligned} A_\epsilon(v, \phi) := & \int_{\Omega_1} \lambda e_{\alpha\alpha}(v(\epsilon)) e_{\beta\beta}(\phi) + 2\mu e_{\alpha\beta}(v(\epsilon)) e_{\alpha\beta}(\phi) dx + \frac{1}{\epsilon^2} \int_{\Omega_1} \lambda e_{\alpha\alpha}(v(\epsilon)) e_{33}(\phi) + \lambda e_{33}(v(\epsilon)) e_{\alpha\alpha}(\phi) dx \\ & + \frac{1}{\epsilon^2} \int_{\Omega_1} 4\mu e_{\alpha 3}(v(\epsilon)) e_{\alpha 3}(\phi) dx + \frac{1}{\epsilon^4} \int_{\Omega_1} (\lambda + 2\mu) e_{33}(v(\epsilon)) e_{33}(\phi) dx, \end{aligned} \quad (\text{B.15})$$

and

$$\begin{aligned} A'_\epsilon(v, \phi) := & \epsilon^2 \int_{\Omega_1} \lambda' e_{\alpha\alpha}(v(\epsilon)) e_{\beta\beta}(v) + 2\mu' e_{\alpha\beta}(v(\epsilon)) e_{\alpha\beta}(v) dx \\ & + \epsilon^2 \int_{\Omega_1} \lambda' e_{\alpha\alpha}(v(\epsilon)) e_{33}(v) + \lambda' (e_{33}(v(\epsilon)) - 2\bar{g}) e_{\alpha\alpha}(v) dx \\ & + \epsilon^2 \int_{\Omega_1} 4\mu' (e_{\alpha 3}(v(\epsilon)) - x_3 \bar{g}_{,\alpha}) e_{\alpha 3}(v) dx \\ & + \int_{\Omega_1} (\lambda' + 2\mu') (e_{33}(v(\epsilon)) - \bar{g}) e_{33}(v) dx. \end{aligned} \quad (\text{B.16})$$

We now consider an expansion of  $v$  in even powers of  $\epsilon$  (odd powers of  $\epsilon$  would trivially cancel in the sequel)

$$v(\epsilon) = v_0 + \epsilon^2 v_2 + \epsilon^4 v_4 + \mathcal{O}(\epsilon^6), \quad (\text{B.17})$$

where  $v_0, v_2, v_4 \in \mathbb{V}$ . Substituting this expression in the first order optimality conditions, we get that

$$\epsilon^{-4} a_{-4}(v, \phi) + \epsilon^{-2} a_{-2}(v, \phi) + a_0(v, \phi) + \mathcal{O}(\epsilon^2) = 0 \quad \forall \phi \in \mathbb{V} \quad (\text{B.18})$$

where

$$a_{-4}(v, \phi) := \int_{\Omega_1} (\lambda + 2\mu) e_{33}(v_0) e_{33}(v) dx \quad (\text{B.19})$$

$$a_{-2}(v, \phi) := \int_{\Omega_1} \lambda (e_{\alpha\alpha}(v_0) e_{33}(v) + e_{33}(v_0) e_{\alpha\alpha}(v)) dx + \int_{\Omega_1} 4\mu e_{\alpha 3}(v_0) e_{\alpha 3}(v) dx + \int_{\Omega_1} (\lambda + 2\mu) e_{33}(v_2) e_{33}(v) dx \quad (\text{B.20})$$

$$\begin{aligned} a_0(v, \phi) := & \int_{\Omega_1} \lambda e_{\alpha\alpha}(v_0) e_{\beta\beta}(v) + 2\mu e_{\alpha\beta}(v_0) e_{\alpha\beta}(v) dx + \int_{\Omega_1} \lambda (e_{\alpha\alpha}(v_2) e_{33}(v) + e_{33}(v_2) e_{\alpha\alpha}(v)) dx \\ & + \int_{\Omega_1} 4\mu e_{\alpha 3}(v_2) e_{\alpha 3}(v) dx + \int_{\Omega_1} (\lambda + 2\mu) e_{33}(v_4) e_{33}(v) dx \\ & + \int_{\Omega_1} (\lambda' + 2\mu') (e_{33}(v_0) - \bar{g}) e_{33}(v) dx \end{aligned} \quad (\text{B.21})$$

Assuming then that convergence takes place at each scale and from the expression of  $a_{-4}$ , it is easy to obtain that

$$e_{33}(v_0) = 0 \quad \text{in } \Omega_1, \quad (\text{B.22})$$

so that

$$a_{-4}(v, \phi) = 0 \quad \forall v \in \mathbb{V}. \quad (\text{B.23})$$

At order  $\epsilon^{-2}$ , we first consider a test function  $v$  in the form  $v(x_\alpha, x_3) = f(x_3)e_3$  with  $f$  continuously differentiable on  $(0, 1)$ . From (B.18) and (B.20), we obtain that

$$\int_{\Omega_1} (\lambda e_{\alpha\alpha}(v_0) + (\lambda + 2\mu)e_{33}(v_2))f' dx = 0,$$

and from the arbitrariness of  $f$ , that

$$e_{33}(v_2) = -\frac{\lambda}{\lambda + 2\mu} e_{\alpha\alpha}(v_0) \text{ in } \Omega_1. \tag{B.24}$$

Combining (B.22), (B.24), and (B.20), we get that  $\int_{\Omega_1} 4\mu e_{\alpha 3}(v_0)e_{\alpha 3}(v)dx = 0$  for all  $v \in V$ , so that

$$e_{\alpha 3}(v_0) = 0 \text{ in } \Omega_1, \tag{B.25}$$

so that

$$a_{-2}(v, \phi) = 0 \quad \forall v \in \mathbb{V}. \tag{B.26}$$

**Remark 3.** Combining (B.22) and (B.25), it is easy to see that  $v_0$  is a Kirchhoff–Love field in  $\Omega_1$ , i.e., that there exists a function  $U_0$  of  $x_\alpha$  such that

$$(v_0)_\alpha = -(x_3 - \frac{1}{2})(v_0)_{3,\alpha}(x_\alpha) + (U_0)_\alpha(x_\alpha), \quad \alpha = 1, 2. \tag{B.27}$$

From (B.22), we deduce that  $(v_0)_3$  depends only on  $x_\alpha$ , so that

$$(v_0)_3 = f(x_\alpha)$$

for some function  $f$ . Accounting then for (B.25), we get that

$$(v_0)_{\alpha,3} = -(v_0)_{3,\alpha} = -\frac{\partial f}{\partial x_\alpha} \quad \text{in } \Omega_1, \quad \alpha = 1, 2,$$

and integrating along the  $x_3$  direction we can obtain (B.27)

$$(v_0)_\alpha = -\left(x_3 - \frac{1}{2}\right) \frac{\partial f}{\partial x_\alpha} + (U_0)_\alpha(x_\alpha) \text{ in } \Omega_1, \quad \alpha = 1, 2,$$

where  $(U_0)_\alpha$  is the in-plane displacement in  $\Omega_1$  on  $x_3 = \frac{1}{2}$  plane.

We finally turn our attention to the terms of order 1. Consider first a test function in the form  $\phi = f(x_3)e_3$ , with  $f \in C_c^\infty(0, 1)$ . Substituting in (B.21), we get that

$$\int_{\Omega_1} (\lambda e_{\alpha\alpha}(v_2) + (\lambda + 2\mu)e_{33}(v_4))f'(x_3) dx = 0,$$

so that

$$e_{33}(v_4) = -\frac{\lambda}{\lambda + 2\mu} e_{\alpha\alpha}(v_2) \text{ in } \Omega_1. \tag{B.28}$$

We then consider a test function in the form  $\phi = f(x_\alpha)e_3$  with  $f(x_\alpha) \in C_c^\infty(0, 1)$ . Again, substitution into (B.21) yields

$$\int_{\Omega_1} 2\mu e_{\alpha 3}(v_2)e_{\alpha 3}(\phi) dx = 0$$

so that

$$e_{\alpha 3}(v_2) = 0 \text{ in } \Omega_1. \tag{B.29}$$

Finally, we consider a third test function in the form  $\phi = f(x_3)e_3$  with  $f(x_3) \in C_c^\infty(-1, 0)$ . Substituting in (B.21), and integrating by parts in the  $x_3$  direction, we get that

$$\begin{aligned} 0 &= \int_{\Omega_1} (\lambda' + 2\mu')(e_{33}(v_0) - \bar{g}(x_\alpha))f'(x_3) dx \\ &= [((v_0)_{3,3}(x_\alpha, 0) - \bar{g}(x_\alpha))f(0) - ((v_0)_{3,3}(x_\alpha, -1) - \bar{g}(x_\alpha))f(-1)] - \int_{\Omega_1} (\lambda' + 2\mu')(v_0)_{3,33}f(x_3) dx. \end{aligned}$$

Since  $f(0) = f(-1) = 0$ , we obtain

$$\int_{\Omega_1} (\lambda' + 2\mu')(v_0)_{3,33}f(x_3) dx = 0,$$

and therefore

$$(v_0)_{3,33} = 0 \text{ in } \Omega_1.$$

Using then the continuity of  $v_0$  at  $x_3 = 0$  (along the interface between film and the cohesive bond), we deduce

$$(v_0)_3 = (1 + x_3)(v_0)_3(x_\alpha, 0^+) \text{ in } \Omega'_1. \quad (\text{B.30})$$

Using (B.23), (B.26) replacing in (B.15) we get

$$\begin{aligned} A(v, \phi) = & \int_{\Omega_1} \lambda e_{\alpha\alpha}(v_0) e_{\beta\beta}(\phi) + 2\mu e_{\alpha\beta}(v_0) e_{\alpha\beta}(\phi) \, dx + \int_{\Omega_1} \lambda (e_{\alpha\alpha}(v_2) e_{33}(\phi) + e_{33}(v_2) e_{\alpha\alpha}(\phi)) \, dx \\ & + \int_{\Omega_1} 4\mu e_{\alpha 3}(v_2) e_{\alpha 3}(\phi) \, dx + \int_{\Omega_1} (\lambda + 2\mu) e_{33}(v_4) e_{33}(\phi) \, dx + O(\epsilon^2) \end{aligned} \quad (\text{B.31})$$

using first (B.28) and (B.29) we get

$$A(v, \phi) = \int_{\Omega_1} \lambda e_{\alpha\alpha}(v_0) e_{\beta\beta}(\phi) + 2\mu e_{\alpha\beta}(v_0) e_{\alpha\beta}(\phi) \, dx + \int_{\Omega_1} \lambda e_{33}(v_2) e_{\alpha\alpha}(\phi) \, dx + O(\epsilon^2) \quad (\text{B.32})$$

finally accounting for (B.24), we get

$$A(v, \phi) = \int_{\Omega_1} \frac{2\mu\lambda}{\lambda + 2\mu} e_{\alpha\alpha}(v_0) e_{\beta\beta}(\phi) + 2\mu e_{\alpha\beta}(v_0) e_{\alpha\beta}(\phi) \, dx + O(\epsilon^2). \quad (\text{B.33})$$

Similarly for (B.16) we get

$$A'(v, \phi) = \int_{\Omega'_1} (\lambda' + 2\mu')(e_{33}(v_0) - \bar{g}) e_{33}(\phi) \, dx + O(\epsilon^2) \quad (\text{B.34})$$

We can derive the asymptotic energy from (B.33) and B.34) as

$$G(u) = \frac{1}{2} \int_{\Omega_1} \frac{2\mu\lambda}{\lambda + 2\mu} e_{\alpha\alpha}(v_0) e_{\beta\beta}(v_0) + 2\mu e_{\alpha\beta}(v_0) e_{\alpha\beta}(v_0) \, dx + O(\epsilon^2) \quad (\text{B.35})$$

$$G'(u) = \frac{1}{2} \int_{\Omega'_1} (\lambda' + 2\mu')(e_{33}(v_0) - \bar{g})(e_{33}(v_0) - \bar{g}) \, dx + O(\epsilon^2). \quad (\text{B.36})$$

Changing variables from  $v$  to  $u$ , integrating in  $x_3$ , and using (B.27) we get

$$G_\epsilon(u) = \frac{1}{2} \int_\Gamma \frac{2\mu\lambda}{12(\lambda + 2\mu)} (u_0)_{3,\alpha\alpha} (u_0)_{3,\beta\beta} + \frac{\mu}{6} (u_0)_{3,\alpha\beta} (u_0)_{3,\alpha\beta} \, dx + \int_\Gamma \frac{2\mu\lambda}{\lambda + 2\mu} e_{\alpha\alpha}(U_0) e_{\beta\beta}(U_0) + 2\mu e_{\alpha\beta}(U_0) e_{\alpha\beta}(U_0) \, dx + O(\epsilon^2) \quad (\text{B.37})$$

where  $u_0 = v_0 + g$  is the leading term for in-homogenous scaled displacement field  $u = v + g$ .

Similarly in  $\Omega'_1$  using (B.30) (taking in account that  $(v_0)_{3,3} = (u_0)_{3,3} = 0$  in  $\Omega_1$ ), we can write

$$G'_\epsilon(u) = \frac{1}{2} \int_\Gamma (\lambda' + 2\mu') |(u_0)_{3,\alpha} - \bar{g}(x_\alpha)|^2 \, dx + O(\epsilon^2), \quad (\text{B.38})$$

where  $\Gamma = (\bullet, \frac{1}{2})$  is film's mid surface and  $U_0$  is the in-plane displacement in  $\Gamma$ . In this particular case since out-of-plane  $((u_0)_3)$  and in-plane  $(U_0)$  terms are decoupled and since there is no loading in the in-plane direction (i.e.,  $g_\alpha = 0$ ) we get

$$F(u) = \frac{1}{2} \int_\Gamma \frac{2\mu\lambda}{12(\lambda + 2\mu)} (u_0)_{3,\alpha\alpha} (u_0)_{3,\beta\beta} + \frac{\mu}{6} (u_0)_{3,\alpha\beta} (u_0)_{3,\alpha\beta} \, dx + \frac{1}{2} \int_\Gamma (\lambda' + 2\mu') |(u_0)_3 - \bar{g}|^2 \, dx + O(\epsilon^2) \quad (\text{B.39})$$

## References

- Ambrosio, L., Tortorelli, V.M., 1990. Approximation of functionals depending on jumps by elliptic functionals via  $\Gamma$ -convergence. *Commun. Pure Appl. Math.* 43 (8), 999–1036.
- Balay, S., Gropp, W.D., McInnes, L.C., Smith, B.F., 1997. Efficient management of parallelism in object oriented numerical software libraries. In: Arge, E., Bruaset, A.M., Langtangen, H.P. (Eds.), *Modern Software Tools in Scientific Computing*. Birkhäuser Press, pp. 163–202.
- Balay, S., Brown, J., Buschelman, K., Eijkhout, V., Gropp, W.D., Kaushik, D., Knepley, M.G., McInnes, L.C., Smith, B.F., Zhang, H., 2012a. PETSc Users Manual, Technical Report. ANL-95/11—Revision 3.3, Argonne National Laboratory.
- Balay, S., Brown, J., Buschelman, K., Gropp, W.D., Kaushik, D., Knepley, M.G., McInnes, L.C., Smith, B.F., Zhang, H., 2012b. PETSc Web page, (<http://www.mcs.anl.gov/petsc>).
- Bourdin, B., 2007. Numerical implementation of the variational formulation for quasi-static brittle fracture. *Interfaces Free Boundaries* 9 (3), 411–430.
- Bourdin, B., Chambolle, A., 2000. Implementation of an adaptive finite-element approximation of the Mumford–Shah functional. *Numer. Math.* 85 (4), 609–646.
- Bourdin, B., Francfort, G.A., Marigo, J.-J., 2008. The variational approach to fracture. *J. Elasticity* 91 (1), 5–148.
- Braides, A., 1998. *Approximation of Free-Discontinuity Problems*, Lecture Notes in Mathematics. Springer-Verlag.
- Chai, H., Lawn, B.R., 2004. Fracture mode transitions in brittle coatings on compliant substrates as a function of thickness. *J. Mater. Res.* 19 (6), 1752–1761.
- Chambolle, A., 1995. Image segmentation by variational methods: Mumford and Shah functional and the discrete approximations. *SIAM J. Appl. Math.* 55 (3), 827–863.
- Chambolle, A., Giacomini, A., Ponsiglione, M., 2008. Crack initiation in brittle materials. *Arch. Ration. Mech. Anal.* 188 (2), 309–349.
- Chen, J., 2012. Indentation-based methods to assess fracture toughness for thin coatings. *J. Phys. D Appl. Phys.* 45 (20), 203001.
- Ciarlet, P., 1997. *Mathematical Elasticity: Theory of Plates*, Studies in Mathematics and its Applications, vol. 27. Elsevier.
- Francfort, G.A., Marigo, J.-J., 1998. Revisiting brittle fracture as an energy minimization problem. *J. Mech. Phys. Solids* 46 (8), 1319–1342.

- Giacomini, A., 2005. Ambrosio–Tortorelli approximation of quasi-static evolution of brittle fractures. *Calculus Variations Partial Differential Equations* 22 (2), 129–172.
- Hakim, V., Karma, A., 2009. Laws of crack motion and phase-field models of fracture. *J. Mech. Phys. Solids* 57 (2), 342–368.
- Henry, H., Levine, H., 2004. Dynamic instabilities of fracture under biaxial strain using a phase field model. *Phys. Rev. Lett.* 93 (10), 105–504.
- Hutchinson, J.W., Suo, Z., 1992. Mixed mode cracking in layered materials. *Adv. Appl. Mech.* 29, 63–191.
- Karma, A., Lobkovsky, A.E., 2004. Unsteady crack motion and branching in a phase-field model of brittle fracture. *Phys. Rev. Lett.* 92 (24), 245–510.
- Lawn, B.R., 1998. Indentation of ceramics with spheres: a century after Hertz. *J. Am. Ceram. Soc.* 81 (8), 1977–1994.
- Lawn, B., Deng, Y., Miranda, P., Pajares, A., Chai, H., Kim, D., 2002. Overview: damage in brittle layer structures from concentrated loads. *J. Mater. Res.* 17 (12), 3019–3036.
- Léon Baldelli, A.A., Bourdin, B., Marigo, J.-J., Maurini, C., 2013. Fracture and debonding of a thin film on a stiff substrate: analytical and numerical solutions of a 1D variational model. *Continuum Mech. Thermodyn.* 25 (2–4), 243–268.
- Maurini, C., Bourdin, B., Gauthier, G., Lazarus, V., 2013. Crack patterns obtained by unidirectional drying of a colloidal suspension in a capillary tube: experiments and numerical simulations using a two-dimensional variational approach. *Int. J. Fracture*, <http://dx.doi.org/10.1007/s10704-013-9824-5>, in press.
- Mesarovic, S.D., Fleck, N.A., 1999. Spherical indentation of elastic–plastic solids. *Proc. R. Soc. London A Math. Phys. Eng. Sci.* 455 (1987), 2707–2728.
- Mishnaevsky, L.L., Gross Jr., D., 2004. Micromechanisms and mechanics of damage and fracture in thin film/substrate systems. *Int. Appl. Mech.* 40 (2), 140–155.
- Morasch, K.R., Bahr, D.F., 2007. An energy method to analyze through thickness thin film fracture during indentation. *Thin Solid Films* 515 (6), 3298–3304.
- Munson, T., Sarich, J., Wild, S., Benson, S., McInnes, L.C., 2012. Tao 2.0 Users Manual, Technical Report. ANL/MCS-TM-322, Mathematics and Computer Science Division, Argonne National Laboratory, (<http://www.mcs.anl.gov/tao>).
- Pham, K., Marigo, J.-J., Maurini, C., 2011. The issues of the uniqueness and the stability of the homogeneous response in uniaxial tests with gradient damage models. *J. Mech. Phys. Solids* 59 (6), 1163–1190.
- Rhee, Y.-W., Kim, H.-W., Deng, Y., Lawn, B.R., 2001. Contact-induced damage in ceramic coatings on compliant substrates: fracture mechanics and design. *J. Am. Ceram. Soc.* 84 (5), 1066–1072.
- Sierros, K.A., Kessman, A.J., Nair, R., Randall, N.X., Cairns, D.R., 2011. Spherical indentation and scratch durability studies of transparent conducting layers on polymer substrates. *Thin Solid Films* 520 (1), 424–429.
- Szilard, R., 2004. *Theories and Applications of Plate Analysis: Classical, Numerical, and Engineering Methods*. Wiley.
- Xia, Z.C., Hutchinson, J.W., 2000. Crack patterns in thin films. *J. Mech. Phys. Solids* 48 (6–7), 1107–1131.
- Zeng, K., Zhu, F., Hu, J., Shen, L., Zhang, K., Gong, H., 2003. Investigation of mechanical properties of transparent conducting oxide thin films. *Thin Solid Films* 443 (1), 60–65.